

See discussions, stats, and author profiles for this publication at: <https://www.researchgate.net/publication/6951727>

# Influence of Monolayer Amounts of $\text{HNO}_3$ on the Evaporation Rate of $\text{H}_2\text{O}$ over Ice in the Range 179 to 208 K: A Quartz Crystal Microbalance Study

ARTICLE *in* THE JOURNAL OF PHYSICAL CHEMISTRY A · AUGUST 2005

Impact Factor: 2.69 · DOI: 10.1021/jp0505072 · Source: PubMed

---

CITATIONS

12

---

READS

47

## 2 AUTHORS:



**Christophe Delval**

Looking for new challenges...

9 PUBLICATIONS 82 CITATIONS

SEE PROFILE



**Michel J Rossi**

Paul Scherrer Institut

259 PUBLICATIONS 6,468 CITATIONS

SEE PROFILE

# Influence of Monolayer Amounts of HNO<sub>3</sub> on the Evaporation Rate of H<sub>2</sub>O over Ice in the Range 179 to 208 K: A Quartz Crystal Microbalance Study

Christophe Delval and Michel J. Rossi\*

Ecole Polytechnique Fédérale de Lausanne (EPFL), Laboratoire de Pollution Atmosphérique et Sol (LPAS), CH-1015 Lausanne, Switzerland

Received: January 28, 2005; In Final Form: May 6, 2005

The evaporation flux  $J_{\text{ev}}$  of H<sub>2</sub>O from thin H<sub>2</sub>O ice films containing between 0.5 and 7 monolayers of HNO<sub>3</sub> has been measured in the range 179 to 208 K under both molecular and stirred flow conditions in isothermal experiments. FTIR absorption of the HNO<sub>3</sub>/H<sub>2</sub>O condensate revealed the formation of metastable  $\alpha$ -NAT (HNO<sub>3</sub>·3H<sub>2</sub>O) converting to stable  $\beta$ -NAT at 205 K. After deposition of HNO<sub>3</sub> for 16–80 s on a 1  $\mu\text{m}$  thick pure ice film at a deposition rate in the range  $(6\text{--}60) \times 10^{12}$  molecules  $\text{s}^{-1}$  the initial evaporative flux  $J_{\text{ev}}(\text{H}_2\text{O})$  was always that of pure ice.  $J_{\text{ev}}(\text{H}_2\text{O})$  gradually decreased with the evaporation of H<sub>2</sub>O and the concomitant increase of the average mole fraction of HNO<sub>3</sub>,  $\chi_{\text{HNO}_3}$ , indicating the presence of an amorphous mixture of H<sub>2</sub>O/HNO<sub>3</sub> that is called complexed or (c)-ice whose vapor pressure is that of pure ice. The final value of  $J_{\text{ev}}$  was smaller by factors varying from 2.7 to 65 relative to pure ice. Depending on the doping conditions and temperature of the ice film the pure ice thickness  $d_{\text{D}}$  of the ice film for which  $J_{\text{ev}} < 0.85J_{\text{ev}}(\text{pure ice})$  varied between 130 and 700 nm compared to the 1000 nm thick original ice film at 208 and 191 K, respectively, in what seems to be an inverse temperature dependence. There exist three different types of H<sub>2</sub>O molecules under the present experimental conditions, namely (a) free H<sub>2</sub>O corresponding to pure ice, (b) complexed H<sub>2</sub>O or c-ice, and (c) H<sub>2</sub>O molecules originating from the breakup of NAT or amorphous H<sub>2</sub>O/HNO<sub>3</sub> mixtures. The significant decrease of  $J_{\text{ev}}(\text{H}_2\text{O})$  with increasing  $\chi_{\text{HNO}_3}$  leads to an increase of the evaporative lifetime of atmospheric ice particles in the presence of HNO<sub>3</sub> and may help explain the occurrence of persistent and/or large contaminated ice particles at certain atmospheric conditions.

## 1. Introduction

It took a long time to unambiguously prove the existence of polar stratospheric clouds (PSC's) by in situ measurements in the lower stratosphere (LS)<sup>1</sup> after they had been proposed to be the seat of heterogeneous chemistry responsible for polar ozone depletion.<sup>2,3</sup> It took an equal length of time to appreciate the importance of cirrus (ice) clouds for the chemical composition of the upper troposphere (UT), their role in climate change notwithstanding. Pure ice in the atmosphere is prevalent as cold clouds such as cirrus clouds and aviation contrails in the UT as well as type II PSC's in the LS, albeit under special meteorological conditions. Cirrus clouds are ubiquitous throughout the UT and at times can cover as much as 40% of the Earth's surface.<sup>4,5</sup> Natural cirrus clouds are composed of ice particles whose characteristic length scale  $d$  is  $>20 \mu\text{m}$  and which occur at typical number densities  $n$  of  $\ll 100 \text{ cm}^{-3}$ , whereas aviation contrails are composed of small ice particles with  $d$  in the range  $0.5\text{--}3 \mu\text{m}$  at  $n = 100\text{--}200 \text{ cm}^{-3}$ .<sup>6</sup> In addition to regulating the hydrological cycle on a global scale, thereby directly affecting the most important greenhouse gas water vapor,<sup>7</sup> the cirrus clouds themselves play a vital role in the global radiative balance.<sup>8</sup> Cirrus cloud and aviation contrails as well as aviation-induced cirrus cloudiness now represent the largest uncertainty factor in assessing future climate change as well as the future impact of aviation.<sup>6</sup> In addition, the presence of ice particles in the UT/LS on a regional or local scale at midlatitudes begs the question of the importance of heterogeneous chemical reactions of atmospheric trace gases occurring on the surface of these

ice particles,<sup>9</sup> thereby affecting the chemical composition of the relevant atmospheric layers that are most important to climate change. Recently, the sensitivity of cloud parameters such as amount, height, optical depth and particle size on the radiative forcing has been assessed and found to be approximately 10 times higher than corresponding changes in CO<sub>2</sub> concentration.<sup>61</sup> Doubling for instance the cloud height of a cirrus cloud leads to a positive radiative forcing of 12 W/m<sup>2</sup> which is enormous with respect to doubling of the CO<sub>2</sub> concentration which itself leads to a radiative forcing of +2 W/m<sup>2</sup>. In turn, doubling the cloud optical depth leads to a negative radiative forcing of −17 W/m<sup>2</sup>. These large values suggest the importance of atmospheric ice particles on global climate.

Lawrence and Crutzen<sup>10</sup> have suggested that the uptake and gravitational redistribution of nitric acid, HNO<sub>3</sub>, by cirrus cloud particles may represent a significant sink of HNO<sub>3</sub> in the UT,<sup>11</sup> much like the well-known denitrification mechanism of HNO<sub>3</sub> from the LS in the context of polar ozone depletion events. Nitric acid is a reservoir species for NO<sub>x</sub><sup>12</sup> and is a ubiquitous trace gas of global importance. Moreover, a depletion of HNO<sub>3</sub> by sedimentation out of certain layers of the UT will lead to a decrease of NO<sub>x</sub><sup>13</sup> which primarily controls ozone, an important greenhouse gas.<sup>14</sup> Typical concentrations of gas-phase HNO<sub>3</sub> in cirrus clouds ranging from 100 to over 1000 ppt have recently been measured using sophisticated airborne instrumentation such as chemical ionization mass spectrometry (CIMS)<sup>11,15</sup> together with other parameters such as relative humidity (rh).<sup>16</sup>

Field measurements revealed the presence of HNO<sub>3</sub> in type I PSC's as stable crystalline nitric acid trihydrate (NAT or

\* Corresponding author. E-mail: michel.rossi@epfl.ch.

$\text{HNO}_3 \cdot 3\text{H}_2\text{O}$  occurring in the LS at high latitudes and as  $\text{HNO}_3$ -laced, sometimes heavy, ice particles in the UT.<sup>17</sup> The concept of an ice particle with a NAT coating at its surface that would prolong its lifetime due to inhibited evaporation of  $\text{H}_2\text{O}$  is a recurrent idea<sup>18</sup> used to explain the presence of ice particles several degrees above the stratospheric ice frost point.<sup>19</sup> A NAT-coating was once suspected to decrease the  $\text{H}_2\text{O}$  vapor pressure of the coated particles<sup>19,20</sup> despite the presence of a pure ice core, or to decrease the uptake coefficient of  $\text{H}_2\text{O}$  on such a particle.<sup>16</sup> The latter situation would lead to an increase of the lifetime of the particle by lowering the rate of evaporation under the constraint that the vapor pressure of ice were preserved. In the case of cirrus clouds, the recent study of Gao and co-workers<sup>16</sup> based on airborne measurements inside cirrus clouds and aviation contrails has led to the conclusion that the observed increase of rh up to 135% of its saturation value below 202 K may be attributed to the presence of a new type of  $\text{HNO}_3$ -containing ice, so-called  $\Delta$ -ice, that has a  $\gamma$  value of  $\text{H}_2\text{O}$  smaller than the one for pure ice, but whose rate or flux of evaporation,  $R_{\text{ev}}$  and  $J_{\text{ev}}$ , respectively, is identical to pure ice. This proposal implies the breakdown of microscopic reversibility and leads to the violation of the second law of thermodynamics, as has been pointed out.<sup>21</sup> Below we will propose a sound interpretation of the observations of Gao et al. that is based on the present laboratory measurements.

The focus of this work is on the kinetics of  $\text{H}_2\text{O}$  evaporation of ice films in the range 179–208 K that are condensed from the vapor phase and that contain small but known amounts of adsorbed  $\text{HNO}_3$ . The main result is that small amounts of  $\text{HNO}_3$  adsorbed on thin ice films significantly decrease  $J_{\text{ev}}$  once the pure ice fraction has evaporated. This leads to a concomitant increase of the evaporative lifetime of the ice particle.

## 2. Experimental Setup

We present results on the evaporation kinetics of  $\text{H}_2\text{O}$  that have been obtained using the reactor equipped with multiple diagnostics whose hardware parameters have been previously given in detail.<sup>22,23</sup> The experimental apparatus itself is schematically represented in Figure 1.

The main change in the experimental setup compared to the version presented in reference<sup>23</sup> is that the reactor is now equipped with two glass dosing tubes (DT) for vapor injection, one for  $\text{H}_2\text{O}$ ,  $\text{DT}_{\text{H}_2\text{O}}$ , the other for  $\text{HNO}_3$ ,  $\text{DT}_{\text{HNO}_3}$ . The latter may be oriented toward the Si-window of the cryostat (position  $\text{DT}_{\text{HNO}_3}^{\text{Si}}$ ) or the quartz crystal microbalance, QCM, sensor (position  $\text{DT}_{\text{HNO}_3}^{\text{QCM}}$ ) depending on where the ice film to be doped is located. This allows the directed deposition of  $\text{HNO}_3$  onto the ice film as shown in Figure 2 for the case  $\text{DT}_{\text{HNO}_3}^{\text{QCM}}$  which has been pursued in the present study in order to avoid the efficient interaction of  $\text{HNO}_3$  with the reactor internal walls, be they Teflon-coated<sup>24,25</sup> or made of stainless steel.

As a reminder, the precision of the temperature reading was  $\pm 0.5$  K. We do not expect a radial temperature gradient on Si (cryostat) and the Au-coated piezo element (QCM) due to the large known thermal conductivity of these elements ( $170\text{--}500 \text{ W m}^{-1} \text{ K}^{-1}$ <sup>26</sup>). In addition, the thermal conductivity of  $I_h$  ice that is obtained between  $227$  and  $5 \text{ W m}^{-1} \text{ K}^{-1}$ <sup>28,29</sup> implies a temperature gradient across the ice film thickness smaller than  $1 \text{ K } \mu\text{m}^{-1}$ ,<sup>27</sup> which may be considered as negligible in the present study.

Characteristic data on the hardware are summarized in Table 1.

The knowledge of the absolute number of molecules of  $\text{H}_2\text{O}$  that are present on the sensor of the QCM are based on

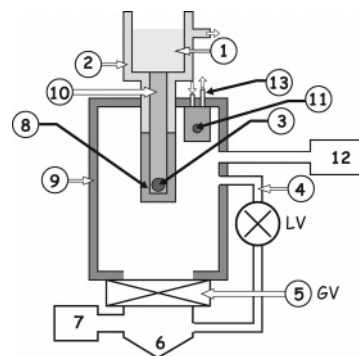


**Figure 1.** Schematic drawing of the experimental apparatus: 1, liquid nitrogen reservoir; 2, evacuated Dewar vessel; 3, silicon window of  $0.78 \text{ cm}^2$  area used as a substrate for  $\text{H}_2\text{O}$  deposition; 4, calibrated leak valve equipped with a leak valve allowing *static* (valve and 5 closed) and *stirred flow or low pumping rate* (valve open and 5 closed) experiments; 5, 6 in. gate valve allowing *dynamic or high pumping rate* experiments when opened; 6, flange for turbo pump; 7, quadrupole mass spectrometer; 8, PTFE thermal insulation isolating the whole cryostat but the Si window; 9, reactor chamber; 10, solid copper finger with cartridge heaters for control of the temperature of the Si substrate; 11, quartz crystal microbalance (QCM) with Delrin insulation preventing significant molecular exchange between the gas phase and the QCM device but the  $0.50 \text{ cm}^2$  piezoelectric crystal itself; 12, absolute pressure gauge (Baratron, MKS 220-AHS). Several type  $T$  thermocouples (not shown here) are located throughout the vacuum side of the cryostat in order to measure the temperature in different areas (Si window, PTFE Insulation, reactor and calibrated leak walls, etc.). In addition, two 2 in. NaCl windows allow the FTIR monitoring of the condensed phase, and two inlet tubes allow the injection of  $\text{H}_2\text{O}$  as well as the trace gas into the reactor; 13, independent temperature controlled cooling of QCM.

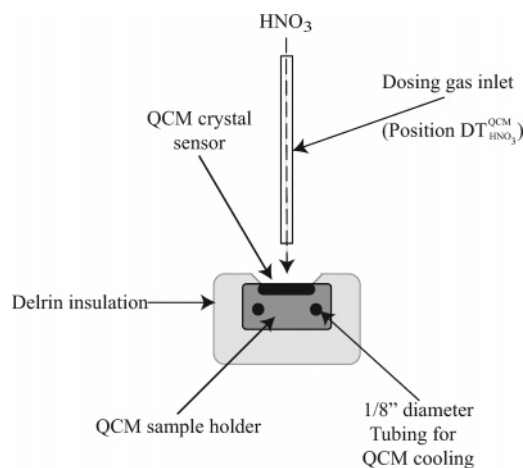


**Figure 2.** Horizontal cut (view from the top) containing the  $\text{HNO}_3$  dosing tube (DT). The Delrin-insulated QCM and the piezoelectric crystal sensor are positioned perpendicular to the reference (paper) plane.

calibrations that are discussed in ref 23. One must remember that these calibrations are mandatory due to the fact that the use of a QCM for the measurement of the mass of any deposit requires the accurate knowledge of the shear modulus of the film. For ice, only scant information has been published on this subject,<sup>30–32</sup> which is the reason we have chosen to independently calibrate the QCM. The cross calibration between the FTIR-probed Si-window and the QCM uses a  $\text{H}_2\text{O}$  ice film deposited from the gas phase at 190 K at a rate of  $5 \times 10^{16}$  to  $1 \times 10^{17} \text{ molecules cm}^{-2} \text{ s}^{-1}$ . This results in a calibration factor for the QCM signal  $C_f = 7.8$  (see Table 1) that leads to a precision of  $1.4 \times 10^{13} \text{ molecules cm}^{-2}$  for the number of  $\text{H}_2\text{O}$  molecules deposited on the QCM sensor element. This roughly

**TABLE 1: Hardware Parameters of Both Cryogenic Sample Supports for the Kinetic Study of HNO<sub>3</sub>-Doped Ice**

	Si optical window <sup>a</sup>	QCM
reactor temp, $T_r$ [K]	320	
reactor vol, $V_r$ [K]	2400	
conversion factor ( $1/RT$ ), Conv [molecules cm <sup>-3</sup> Torr <sup>-1</sup> ]	$3.0 \times 10^{16}$	
sample surface area [cm <sup>2</sup> ]	0.78	0.50
H <sub>2</sub> O collision frequency with ice sample, $\omega_{\text{H}_2\text{O}}$ [s <sup>-1</sup> ]	4.98	3.19
H <sub>2</sub> O effusion rate constant of calibrated leak, $k_{\text{esc}}(\text{H}_2\text{O})$ [s <sup>-1</sup> ]	0.064	
MS calibration factor for H <sub>2</sub> O ( $m/z = 18$ , stirred flow), $C_{18}^{\text{s-flow}}$ [molecules s <sup>-1</sup> A <sup>-1</sup> ]	$2.4 \times 10^{24}$	
MS calibration factor for H <sub>2</sub> O ( $m/z = 18$ , dynamic), $C_{18}^{\text{dyn}}$ [molecules s <sup>-1</sup> A <sup>-1</sup> ]	$1.7 \times 10^{25}$	
HNO <sub>3</sub> collision frequency with ice sample, $\omega_{\text{HNO}_3}$ [s <sup>-1</sup> ]	2.67	1.71
HNO <sub>3</sub> effusion rate constant of calibrated leak, $k_{\text{esc}}(\text{HNO}_3)$ [s <sup>-1</sup> ]	0.042	
MS calibration factor for HNO <sub>3</sub> ( $m/z = 30$ , stirred flow), $C_{30}^{\text{s-flow}}$ [molecules s <sup>-1</sup> A <sup>-1</sup> ]	$6.2 \times 10^{25}$	
MS calibration factor for HNO <sub>3</sub> ( $m/z = 30$ , dynamic), $C_{30}^{\text{dyn}}$ [molecules s <sup>-1</sup> A <sup>-1</sup> ]	$2.2 \times 10^{25}$	
calculated escape orifice area, $A_{\text{esc}}$ [mm <sup>2</sup> ]	1.0	

calibration factor for QCM	
temp [K]	$C_f$ [au]
170	9.0
180	8.0
190	7.8
193	6.0
205	2.0
208	1.9

<sup>a</sup> OD = 1.08 from FTIR for a 10000 Å thick pure ice film.<sup>22</sup>

corresponds to 1.5% of a formal monolayer. These calibrations enable the monitoring of the mass change or growth of a deposited ice film of known initial thickness and film density of 0.93 g cm<sup>-3</sup><sup>33</sup> on the QCM that is subsequently used as a substrate for HNO<sub>3</sub> deposition.

The absolute amount of HNO<sub>3</sub> adsorbed on the ice film is evaluated by first establishing the absolute flow rate of HNO<sub>3</sub>,  $F_r(\text{HNO}_3)$ , into the chamber under stirred flow conditions (gate valve closed, leak valve open) using MS at  $m/z = 30$ .<sup>22</sup> Second, the calibrated MS signal corresponding to the measured HNO<sub>3</sub> loss by adsorption on the ice substrate was integrated in order to determine the absolute number of deposited HNO<sub>3</sub> molecules. In Appendix A, we briefly recall this method described in detail previously<sup>22</sup> but apply it to HNO<sub>3</sub>, instead of HCl and HBr, as well as give the reader information on the calibration of the MS signal under dynamic pumping conditions.

In all kinetic experiments performed between 179 and 208 K the ice film was 1 μm thick and was first grown by deposition of bidistilled water vapor under static conditions (gate valve, leak valve closed, see Figure 1) on the 0.5 cm<sup>2</sup> surface of the QCM sensor at 190 K and a typical rate of  $1 \times 10^{17}$  molecules cm<sup>-2</sup> s<sup>-1</sup>. Such ice films consist of thermodynamically stable polycrystalline ice  $I_h$ <sup>22,34,35</sup> and a thickness of 1 μm ensured a homogeneous coating of ice covering the substrate. Moreover, we have checked that the ice films formed under these conditions are nonporous<sup>22</sup> as expected.<sup>34,36</sup> Indeed, the absence in the FTIR spectrum in transmission of the H<sub>2</sub>O dangling OH-stretch absorption tends to prove that the ice is of low porosity.<sup>37</sup> Subsequently, the ice film temperature is set to the value of interest at stirred flow condition and steady-state H<sub>2</sub>O evaporation is achieved in the upper chamber of the reactor. HNO<sub>3</sub> is then deposited on the ice surface through the directed gas inlet. As soon as the chosen dose of HNO<sub>3</sub> molecules is dispensed, the system is set to dynamic conditions by opening the gate valve in order to halt HNO<sub>3</sub> dosing (Figure 3, point E). Starting from  $t_e$  the HNO<sub>3</sub> doped ice sample evaporation history is tracked and recorded using the QCM as well as MS.

Under the present molecular flow conditions no condensation of water onto the temperature-controlled piezoelectric sensor is taking place owing to the low partial pressure of H<sub>2</sub>O.  $J_{\text{ev}}$  is

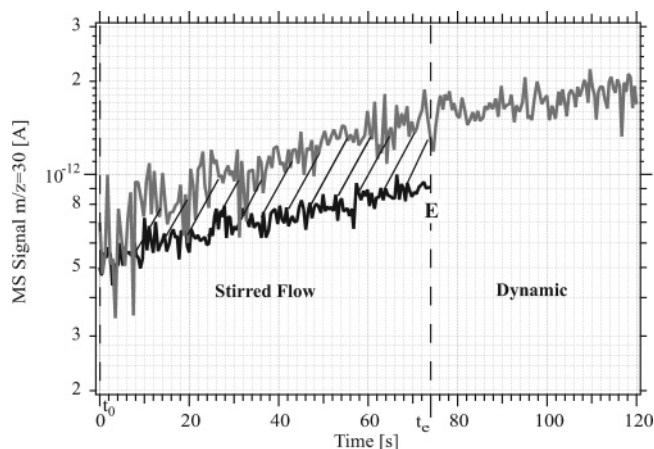


**Figure 3.** Typical MS signals for  $m/z = 30$  during directed HNO<sub>3</sub> admission onto the quartz sensor of the QCM: reference experiment with QCM at 320 K (grey trace) and HNO<sub>3</sub> dosing at 189 K on an ice film (black trace) deposited on the QCM. After the deposition on ice (black trace), the system is set from stirred flow to dynamic conditions at  $t = t_e$  in order to halt HNO<sub>3</sub> admission into the reactor.

therefore directly evaluated from the derivative of the time dependent thickness or number of H<sub>2</sub>O molecules present on the crystal as described in detail in ref 23 following eq 1:

$$J_{\text{ev}} = C_f \times 3.11 \times 10^{14} \times \frac{dS_{\text{QCM}}^{\text{dyn}}}{dt} \times 100 \quad (1)$$

where  $S_{\text{QCM}}^{\text{dyn}}$  is the initial raw output signal in V given by the IC/5 controller,  $C_f = 7.8$  the calibration factor of the QCM for an ice film deposited under the conditions of this work and  $3.11 \times 10^{14}$  [molecules cm<sup>-2</sup> Å<sup>-1</sup>] the number of molecules forming a 1 cm<sup>2</sup> by 1 Å thick ice film of density 0.93.<sup>33</sup> The factor of 100 in eq 1 corresponds to the conversion of the initial IC/5 output voltage of 10 V for a thickness of 1000 Å of a material of unity density and Z-ratio, the acoustic impedance ratio derived from the shear modulus of the deposited thin film.<sup>38</sup> Validation and limits of the quantitative aspects of the QCM technique for pure ice films have been discussed before in ref 23.



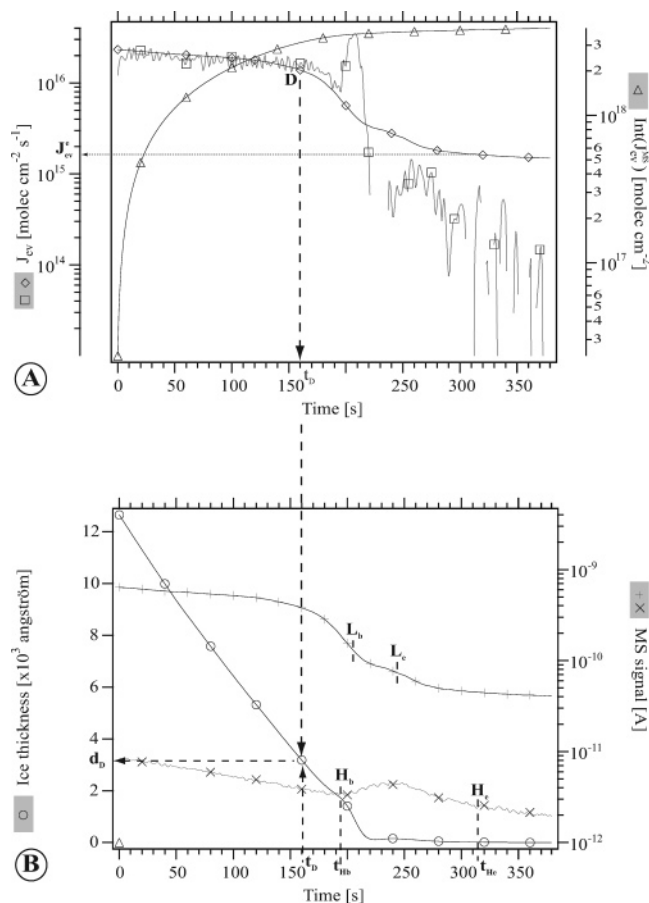


**Figure 4.** Typical experimental protocol of the evaporation at 189 K of a  $1.2 \mu\text{m}$  thick ice film doped with approximately 5 monolayers of  $\text{HNO}_3$ . This illustration corresponds to the experiment whose  $\text{HNO}_3$  deposition and evaporation are described in Figures 3 and 18, respectively: (O) ice thickness monitored by QCM ( $\text{\AA}$ ); ( $\square$ ) “apparent”  $\text{H}_2\text{O}$  evaporative flux,  $J_{ev}^{\text{QCM}}$ , monitored by QCM ( $\text{molecules cm}^{-2} \text{s}^{-1}$ ); (+)  $I_{18}$  MS signal for  $\text{H}_2\text{O}$  (A); ( $\times$ )  $I_{30}$  MS signal for  $\text{HNO}_3$  (A); ( $\diamond$ )  $J_{ev}^{18}$  evaporative flux calculated from  $I_{18}$  ( $\text{molecules cm}^{-2} \text{s}^{-1}$ ); ( $\triangle$ )  $\text{Int}(J_{ev}^{18})$  time integral of  $J_{ev}^{18}$  ( $\text{molecules cm}^{-2}$ ). Different labels correspond to specific instants during ice evaporation described in the text.

### 3. Experimental Method and Results

Figure 4 illustrates a typical evaporation history of a  $1.2 \mu\text{m}$  thick ice film grown at 190 K from the deposition of bidistilled water vapor at a rate of  $1 \times 10^{17} \text{ molecules cm}^{-2} \text{s}^{-1}$  under static conditions. The system was subsequently set to 189 K under stirred flow conditions and  $\text{HNO}_3$  was deposited at an average rate of  $2.2 \times 10^{13} \text{ molecules s}^{-1}$  during 74 s. At  $t = t_{\text{dyn}} = 0 \text{ s}$  in Figure 4, the system was set to molecular flow conditions by opening the gate valve. In this experiment  $1.7 \times 10^{15}$  molecules of  $\text{HNO}_3$  were deposited onto the ice film which approximately corresponds to 5 formal monolayers. From the beginning of the evaporation of the ice film to point D at 189 K in Figure 4 the evaporative flux  $J_{ev}$  is nearly constant and equal to  $2.2 \times 10^{16} \text{ molecules cm}^{-2} \text{s}^{-1}$  which indicates that  $J_{ev}$  remains that of pure ice in agreement with the results we have published previously for the kinetics of evaporation of pure and HX-doped ice<sup>22,23,39</sup> as well as with results from the literature.<sup>40</sup>

At point D, which is evaluated at a precision within 15%,  $J_{ev}$  measured using the QCM,  $J_{ev}^{\text{QCM}}$ , begins to decrease. This apparent change in evaporative flux of  $\text{H}_2\text{O}$  is confirmed by the change of the MS signal at  $m/z = 18$  which follows the same decreasing trend. However,  $J_{ev}^{\text{QCM}}$  and  $I_{18}$  do not change

to the same extent so that we suspect a change of  $C_f$  to occur due to the presence of  $\text{HNO}_3$ . This discrepancy between  $J_{ev}^{\text{QCM}}$  and  $J_{ev}$  obtained from the MS signal at  $m/z = 18$  has been found before and presented in the case of pure ice films.<sup>23</sup> Previously, we have attributed this sudden discrepancy to a probable structural change for a film thickness smaller than 80 nm. This may lead to a modification of the mechanical properties of the ice films and thus of  $C_f$  once the film is thinning out. This may be caused by the probable impact of the roughness of the gold coating of the QCM sensing element. In the present study we take note that the presence of  $\text{HNO}_3$  at doses even smaller than one formal monolayer (see Table 2) leads to a nonlinear change of  $C_f$  occurring at a thickness smaller than  $d_D$  and will not be pursued further in this work. However, the evaporation kinetics of pure ice films presented in Table 2 agree perfectly with results presented in ref 23.

We have extrapolated the diffusion coefficient for  $\text{HNO}_3$  in ice obtained for the range 238–265 K by Thibert and Dominé,<sup>41</sup>  $D = 1.37 \times 10^{-26/10/T} \text{ cm}^2 \text{s}^{-1}$  to the present range of temperatures. This may be regarded as a lower limit for diffusion as their work deals with single-crystal ice whereas our films are polycrystalline. At 189 K, the extrapolated value of  $D = 2.1 \times 10^{-14} \text{ cm}^2 \text{s}^{-1}$  results in a  $\text{HNO}_3$  diffusion time across 25 % of the ice film thickness larger by at least a factor of 40 than the duration of the evaporation experiment. This essentially excludes the possibility for  $\text{HNO}_3$  molecules to reach the surface of the piezoelectric crystal by diffusion. Therefore, the change in  $C_f$  must be due to the change of the mechanical properties of ice doped with  $\text{HNO}_3$  and most probably not due to the presence of  $\text{HNO}_3$  on the gold coated sensor surface. Whatever the reason, it was not the aim of this work to elucidate the reasons for the mismatch between  $J_{ev}^{\text{QCM}}$  and  $J_{ev}$  evaluated from the gas-phase  $\text{H}_2\text{O}$  concentration monitored at  $m/z = 18$ . We claim that QCM data are trustworthy from  $t = t_{\text{dyn}} = 0$  to point D in Figure 4 such that the QCM signal may be used to obtain the mass or thickness of the pure ice film not affected by the presence of  $\text{HNO}_3$  as well as the remaining volume of ice whose kinetics of  $\text{H}_2\text{O}$  evaporation is subsequently affected by the presence of  $\text{HNO}_3$ . This pure ice thickness is denoted as  $d_D$  in Figure 4.

From point D onward the rate of change of the ice thickness corresponding to the evaporative flux of  $\text{H}_2\text{O}$  from ice,  $J_{ev}$ , may be evaluated from the MS signal intensity at  $m/z = 18$  and is called  $J_{ev}^{18}$ . First, we have established the ratio,  $r_{\text{QCM}}^{18}$ , between  $J_{ev}^{\text{QCM}}$  and the analogous flux  $J_{ev}^{18}$  at the beginning of the evaporation. As  $J_{ev}^{\text{QCM}}$  pertains to pure ice and  $C_f$  is constant during the period of pure ice evaporation for  $t < t_D$  we may express  $r_{\text{QCM}}^{18}$  as follows:

$$r_{\text{QCM}}^{18} = \frac{I_{18}}{J_{ev}^{\text{QCM}}} \quad (2)$$

This definition implies that  $r_{\text{QCM}}^{18}$  is a constant between  $t_{\text{dyn}}$  and  $t_D$  as both  $J_{ev}^{\text{QCM}}$  and  $I_{18}$  track each other and reflect the true evaporative flux of  $\text{H}_2\text{O}$  from pure ice up to point D.

Starting at  $t_{\text{dyn}}$  we have calculated the true evaporative flux  $J_{ev}^{18}$  from  $I_{18}$  for thicknesses lower than  $d_{\text{QCM}}(t_{\text{dyn}})$  using eq 3:

$$J_{ev}^{18} = \frac{I_{18}}{r_{\text{QCM}}^{18}} \quad (3)$$

The resulting signal is represented in Figure 4 by symbol  $\diamond$  and is significantly different from  $J_{ev}^{\text{QCM}}$  labeled by symbol  $\square$  for  $t > t_D$ .

**TABLE 2: Representative Experimental Results for the Kinetics of H<sub>2</sub>O Evaporation of Ice Generated from Vapor-Phase Condensation at 190 K in the Presence of HNO<sub>3</sub> for Three Temperature Ranges and Different Deposition Conditions, Where the Symbols of the Third Column Refer to the Corresponding Figures Listed in the Second Column as Well as to the Corresponding Numbers Used in Figures 11–14.**

<i>T</i> range [K]	figure	symbol and no.	<i>T</i> <sub>ice</sub> [K]	<i>R</i> <sub>HNO<sub>3</sub></sub> [molecules s <sup>-1</sup> ]	<i>t</i> <sub>dep</sub> [s]	<i>N</i> <sub>HNO<sub>3</sub></sub> <sup>dep</sup> [molecule] <sup>a</sup>	<i>N</i> <sub>HNO<sub>3</sub></sub> <sup>evap</sup> [molecule] <sup>a</sup>	<i>r</i> <sub>18</sub> <sup>QCM</sup> [Å cm <sup>2</sup> s molecule <sup>-1</sup> ]	<i>d</i> <sub>D</sub> [Å]	<i>J</i> <sub>ev</sub> <sup>b</sup> [molecules cm <sup>-2</sup> s <sup>-1</sup> ]	<i>J</i> <sub>ev</sub> <sup>c</sup> [molecules cm <sup>-2</sup> s <sup>-1</sup> ]	<i>r</i> <sup>b/c</sup>
189–195, range 1	7		192			pure ice		$9.1 \times 10^{-27}$	853	$4.0 \times 10^{16}$		
		○ 1	191	$7.9 \times 10^{12}$	16	$1.5 \times 10^{14}$	$3.2 \times 10^{14}$	$9.0 \times 10^{-27}$	1626	$3.8 \times 10^{16}$	$1.7 \times 10^{15}$	22.3
		△ 2	190	$2.0 \times 10^{13}$	22	$4.7 \times 10^{14}$	$4.4 \times 10^{14}$	$2.3 \times 10^{-26}$	1270	$3.0 \times 10^{16}$	$9.7 \times 10^{14}$	30.9
		□ 3	193	$2.1 \times 10^{13}$	42	$9.4 \times 10^{14}$	$1.4 \times 10^{15}$	$1.6 \times 10^{-26}$	2826	$4.8 \times 10^{16}$	$1.9 \times 10^{15}$	25.3
		▽ 4	191	$2.9 \times 10^{13}$	80	$2.2 \times 10^{15}$	$2.2 \times 10^{15}$	$1.5 \times 10^{-26}$	6970	$4.0 \times 10^{16}$	$7.1 \times 10^{15}$	5.6
		⊕ 5	195	$3.1 \times 10^{12}$	17	$4.0 \times 10^{13}$	$2.6 \times 10^{13}$	$2.9 \times 10^{-26}$	2190	$5.0 \times 10^{16}$	$3.0 \times 10^{15}$	16.7
		⊗	193		44		$2.9 \times 10^{14}$	$3.0 \times 10^{-26}$	3058	$4.9 \times 10^{16}$	$2.3 \times 10^{15}$	21.3
		× 6	189	$1.9 \times 10^{13}$	51	$9.5 \times 10^{14}$	$2.2 \times 10^{15}$	$2.3 \times 10^{-26}$	3458	$2.4 \times 10^{16}$	$1.9 \times 10^{15}$	12.6
		7	189	$3.1 \times 10^{13}$	75	$2.4 \times 10^{15}$			2426			
		◇ 8	189	$2.2 \times 10^{13}$	74	$1.7 \times 10^{15}$	$1.8 \times 10^{15}$	$2.5 \times 10^{-26}$	3089	$2.2 \times 10^{16}$	$1.6 \times 10^{15}$	13.7
179–185, range 2	fig. 8	△ 11	181	$1.8 \times 10^{13}$	32	$5.9 \times 10^{14}$	$3.3 \times 10^{14}$	$2.9 \times 10^{-26}$	4524	$7.0 \times 10^{15}$	$1.0 \times 10^{15}$	7.0
		● 12	180	$5.5 \times 10^{12}$	44	$2.4 \times 10^{14}$	$3.3 \times 10^{14}$	$5.2 \times 10^{-26}$	4786	$6.0 \times 10^{15}$	$9.3 \times 10^{14}$	6.4
		○ 13	184	$1.7 \times 10^{13}$	32	$5.4 \times 10^{14}$	$5.5 \times 10^{14}$	$2.8 \times 10^{-26}$	3709	$9.0 \times 10^{15}$	$1.2 \times 10^{15}$	7.5
		⊕ 14	180	$1.4 \times 10^{13}$	30	$4.3 \times 10^{14}$		$2.5 \times 10^{-26}$	3255	$4.8 \times 10^{15}$	$1.8 \times 10^{15}$	2.7
		⊗ 15	185	$1.9 \times 10^{13}$	64	$1.2 \times 10^{15}$	$1.8 \times 10^{15}$	$3.2 \times 10^{-26}$	5103	$1.2 \times 10^{16}$	$3.6 \times 10^{14}$	33.3
		× 16	181	$1.6 \times 10^{13}$	23	$3.6 \times 10^{14}$		$3.1 \times 10^{-26}$	4787	$4.0 \times 10^{15}$	$1.1 \times 10^{15}$	3.6
		□ 17	179	$1.4 \times 10^{13}$	31	$4.9 \times 10^{14}$	$6.0 \times 10^{14}$	$1.9 \times 10^{-26}$	3568	$6.0 \times 10^{15}$	$4.0 \times 10^{14}$	15.0
		◇ 18	185	$2.1 \times 10^{13}$	60	$1.4 \times 10^{15}$	$1.9 \times 10^{15}$	$2.5 \times 10^{-26}$	1984	$1.2 \times 10^{16}$	$3.6 \times 10^{14}$	33.3
205–208, range 3	fig. 9	⊕ 21	207	$3.0 \times 10^{13}$	60	$1.8 \times 10^{15}$		$4.0 \times 10^{-26}$	3709	$2.2 \times 10^{17}$	$3.4 \times 10^{15}$	64.7
			205			pure ice		$3.4 \times 10^{-26}$	864	$2.0 \times 10^{17}$		
		○ 22	207	$5.6 \times 10^{12}$	66	$4.1 \times 10^{14}$	$8.4 \times 10^{14}$	$2.5 \times 10^{-26}$	2000	$3.0 \times 10^{17}$	$5.0 \times 10^{15}$	60.0
		⊗ 23	208	$6.2 \times 10^{12}$	60	$3.2 \times 10^{14}$	$1.7 \times 10^{14}$	$2.3 \times 10^{-26}$	1196	$3.2 \times 10^{17}$	$5.6 \times 10^{15}$	57.1

<sup>a</sup> Explained in Appendix A.

Because  $J_{ev}^{QCM}$  does not correspond to the true evaporation rate for  $t > t_D$ , the calculated thickness of the film present on the crystal sensor and monitored by the QCM signal is erroneous. Knowledge of the remaining number of H<sub>2</sub>O molecules at any given instant may be obtained from the thickness of the film given by the QCM at  $t = t_{dyn} = 0$  or  $d_{QCM}(t_{dyn})$ , and from  $J_{ev}^{18}$  as a function of time as described in the following.

In Figure 4, symbol △ represents the integral amount of H<sub>2</sub>O molecules per cm<sup>2</sup> at time  $t$  that have desorbed from the ice substrate between  $t_{dyn}$  and  $t$ . This signal, namely  $\text{Int}(J_{ev}^{18})$ , corresponds to the time integral of  $J_{ev}^{18}$  expressed in eq 4:

$$\text{Int}(J_{ev}^{18})(t) = \int_{t_{dyn}}^t J_{ev}^{18}(t) dt \quad (4)$$

The absolute number of H<sub>2</sub>O molecules that are present on the crystal sensor of the QCM,  $N_{H_2O}$ , at time  $t$  may be calculated using eq 5:

$$\begin{aligned} N_{H_2O}(t) &= N_{H_2O}(t_{dyn}) - \text{Int}(J_{ev}^{18})(t) \times A_{QCM} \\ &= d_{QCM}(t_{dyn}) \times 3.11 \times 10^{14} \times A_{QCM} - \text{Int}(J_{ev}^{18})(t) \times A_{QCM} \quad (5) \end{aligned}$$

where  $N_{H_2O}(t_{dyn})$  is the number of molecules present on the sensor at  $t = t_{dyn}$  when the system is set from static to dynamic flow conditions,  $A_{QCM} = 0.5 \text{ cm}^2$  is the effective surface of the QCM sensing element and  $d_{QCM}(t_{dyn})$  the true thickness given at  $t_{dyn}$  by the QCM taking into account the calibration factor  $C_f = 7.8$ .

The calculated absolute number of H<sub>2</sub>O molecules present on the QCM during evaporation,  $N_{H_2O}(t)$ , is represented in Figure 5 by symbol ⊗ and the thickness,  $d_{QCM}(t)$ , given by the QCM is labeled by symbol ○, the different scales notwithstanding. As expected, the signals ⊗ and ○ track each other from  $t_{dyn}$  up to  $t_D = 160 \text{ s}$ , corresponding to point D in Figure 4 and thickness  $d_D$ .

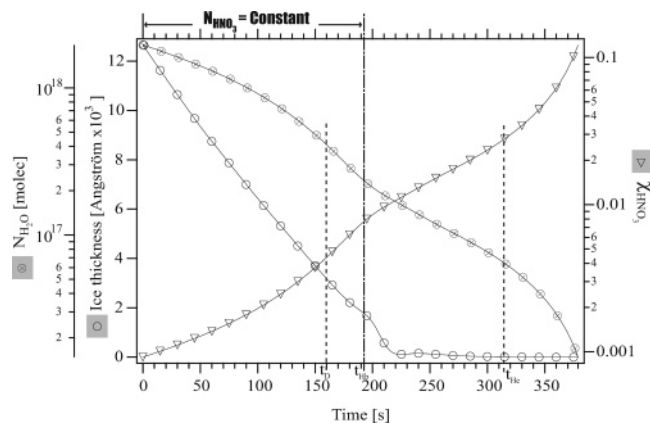


**Figure 5.** Profile of the evolution of the average mole fraction of HNO<sub>3</sub> at 189 K,  $\chi_{HNO_3}$ , in the ice film treated in Figure 4 during water evaporation: (○) thickness given by the QCM,  $d_{QCM}(t)$ ; (⊗) true number of H<sub>2</sub>O molecules on the QCM calculated using eq 5; (▽) resulting  $\chi_{HNO_3}(t)$  under the assumption of constant  $N_{HNO_3}$  (no HNO<sub>3</sub> evaporation observable) and uniform [HNO<sub>3</sub>] throughout the whole ice film.

There is no release of HNO<sub>3</sub> prior to the point labeled H<sub>b</sub> at  $t_{Hb}$  as displayed in Figure 4. Indeed, in all the experiments presented in this work HNO<sub>3</sub> always evaporates at the end of ice film sublimation. This preferential desorption of H<sub>2</sub>O molecules under conditions of H<sub>2</sub>O undersaturation and in the presence of HNO<sub>3</sub> has been observed before.<sup>42,48</sup> As a consequence, the number of HNO<sub>3</sub> molecules present on the ice substrate,  $N_{HNO_3}(t)$  may be considered to be constant up to  $t_{Hb}$ , the point of appearance of HNO<sub>3</sub> desorption monitored at  $m/z = 30$ .

Although we know that HNO<sub>3</sub> is not of uniform concentration in the ice film the average value of  $\chi_{HNO_3}$  may be regarded as a useful measure of the amount of adsorbed HNO<sub>3</sub> in view of the changing amount of H<sub>2</sub>O owing to evaporation. The present experiments were not designed to provide information on the concentration profile of HNO<sub>3</sub> which would be required to obtain a depth-resolved value of  $\chi_{HNO_3}(t)$ .

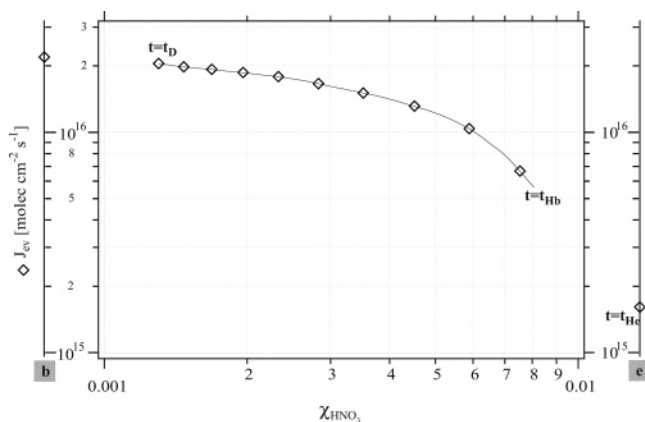


**Figure 6.** Dependence of the evaporative flux of H<sub>2</sub>O,  $J_{\text{ev}}$ , on  $\chi_{\text{HNO}_3}$ , for the sample used in Figures 4 and Figure 5 for the time interval  $t_D$  to  $t_{\text{Hb}}$ . The initial value of  $\chi_{\text{HNO}_3}$  at  $t_{\text{dyn}} = 0$  was  $8.5 \times 10^{-4}$ . The significance of the axes with the second label “b” and “e” is explained in the text.

We have calculated the average mole fraction of HNO<sub>3</sub> in ice as a function of time,  $\chi_{\text{HNO}_3}(t)$ , up to  $t_{\text{Hb}}$  which implies uniform concentration of HNO<sub>3</sub> throughout the remaining ice film. By definition

$$\chi_{\text{HNO}_3}(t) = \frac{N_{\text{HNO}_3}(t_{\text{dyn}})}{N_{\text{H}_2\text{O}}(t) + N_{\text{HNO}_3}(t_{\text{dyn}})} \quad (6)$$

with  $N_x$  the total number of molecules of species  $x$  in the film.

In the present work  $N_{\text{HNO}_3}$  is always smaller than  $3 \times 10^{15}$  molecules for all experiments we have performed. Consequently,  $\chi_{\text{HNO}_3}$  was calculated using the simplified eq 7 because  $N_{\text{H}_2\text{O}} \gg N_{\text{HNO}_3}$  for  $d > 50$  nm:

$$\begin{aligned} \chi_{\text{HNO}_3}(t) &= \frac{N_{\text{HNO}_3}(t_{\text{dyn}})}{N_{\text{H}_2\text{O}}(t)} \\ &= \frac{N_{\text{HNO}_3}(t_{\text{dyn}})}{d_{\text{QCM}}(t_{\text{dyn}}) \times 3.11 \times 10^{14} \times A_{\text{QCM}} - \text{Int}(J_{\text{ev}}^{18})(t) \times A_{\text{QCM}}} \end{aligned} \quad (7)$$

The resulting average mole fraction as a function of time,  $\chi_{\text{HNO}_3}(t)$  for the experiment presented in Figure 4 is displayed in Figure 5 using the  $\nabla$  symbol. One must note that  $\chi_{\text{HNO}_3}(t)$  is only strictly valid for the range  $t_{\text{dyn}} = 0$  to  $t_{\text{Hb}} = 192$  s as specified in Figures 4 and 5, the latter of which corresponds to the time where HNO<sub>3</sub> desorption starts to be observable using MS. Indeed, we have considered  $N_{\text{HNO}_3}$  as constant for the calculation of the average mole fraction of HNO<sub>3</sub>,  $\chi_{\text{HNO}_3}$ , in the evaporating ice film.

The main goal of the present work is to investigate the dependence of the evaporative flux  $J_{\text{ev}}$  of H<sub>2</sub>O on the average value of  $\chi_{\text{HNO}_3}(t)$ . We have therefore exchanged the time against the  $\chi_{\text{HNO}_3}$  scale for evaporative flux data  $J_{\text{ev}}$ . From now on,  $J_{\text{ev}}$  will always refer to  $J_{\text{ev}}^{18}$ , the evaporative flux of H<sub>2</sub>O from ice evaluated using the MS signal at  $m/z = 18$  displayed as a function of the relative concentration  $\chi_{\text{HNO}_3}$ .

Figure 6 displays the results of  $J_{\text{ev}} = f(\chi_{\text{HNO}_3})$  for the experiment presented in Figures 4 and 5. It illustrates the decrease of  $J_{\text{ev}}$  with increasing  $\chi_{\text{HNO}_3}$  in an ice film condensed at 190 K and subsequently doped with  $1.7 \times 10^{15}$  molecules of HNO<sub>3</sub> at 189 K under stirred flow conditions at a rate of  $2.2 \times 10^{13}$  molecules s<sup>-1</sup> before the system is set to molecular flow conditions at  $t_{\text{dyn}}$ . For the purpose of clarity the initial value of

$J_{\text{ev}}$  at the beginning of the evaporation of the ice film at  $t_{\text{dyn}}$  has been reported on the left axis labeled “b” in Figure 6. In addition, the right axis labeled “e” stands for the value of  $J_{\text{ev}}$  toward the end of the evaporation after the desorption of most of the adsorbed HNO<sub>3</sub>, that is at  $t_{\text{He}}$  corresponding to point H<sub>e</sub> in Figure 4.

The value of  $J_{\text{ev}}^b = 2.2 \times 10^{16}$  molecules cm<sup>-2</sup> s<sup>-1</sup> at  $t_{\text{dyn}}$  when  $\chi_{\text{HNO}_3}$  is the smallest, that is approximately  $8.5 \times 10^{-4}$ , is in perfect agreement with previously published data for pure ice.<sup>23</sup> It tends to confirm that small amounts of HNO<sub>3</sub>, corresponding to  $\chi_{\text{HNO}_3} \leq 8.5 \times 10^{-4}$  in this example, do not affect the kinetics of H<sub>2</sub>O evaporation from ice.<sup>18,43</sup> This is true only for the beginning of the evaporation process because the impact of HNO<sub>3</sub> doping on  $J_{\text{ev}}$  becomes increasingly significant as  $\chi_{\text{HNO}_3}$  increases as displayed in Figure 6. According to Figure 6, a decrease of a factor of 2 in  $J_{\text{ev}}$  already occurs for  $\chi_{\text{HNO}_3} = 5.6 \times 10^{-3}$ , which corresponds to a remaining ice film thickness of 193 nm. Figure 6 displays  $J_{\text{ev}}$  in the time span  $t_D$  to  $t_{\text{Hb}}$  corresponding to the displayed variation in  $\chi_{\text{HNO}_3}$ . The dependence of  $J_{\text{ev}}$  from  $t_{\text{dyn}} = 0$  at  $\chi_{\text{HNO}_3} = 8.5 \times 10^{-4}$  to  $t_D$  corresponding to the first point in Figure 6 is not explicitly shown even though it covers a substantial mass fraction of the film evaporation. However, in this work we intend to focus on the time domain where  $\chi_{\text{HNO}_3}$  changes most, that is between  $t_D$  and  $t_{\text{Hb}}$ .

During H<sub>2</sub>O evaporation from HNO<sub>3</sub>-contaminated ice  $J_{\text{ev}}$  steadily decreases down to the value reported on the axis labeled “e”. This continuous decrease of  $J_{\text{ev}}$  with the increase of  $\chi_{\text{HNO}_3}$  has already been reported in ref 22 for the cases of HCl and HBr doping. We have chosen to display  $J_{\text{ev}}^e$ , the smallest evaporative flux of H<sub>2</sub>O from ice based on  $I_{18}$  just before the end of the observable evaporation of HNO<sub>3</sub> at  $t_{\text{He}}$  corresponding to point H<sub>e</sub> in Figure 4. Indeed, in most of the experiments reported in the present work,  $J_{\text{ev}}$  varies at a slower rate from  $t_{\text{Hb}}$  to  $t_{\text{He}}$  compared to the initial rate as displayed in Figure 5 (symbol  $\otimes$ ). As will be discussed below we attribute this more slowly varying portion of  $J_{\text{ev}}(t)$  displayed in Figure 5 to the decomposition of NAT between  $t_{\text{Hb}}$  and  $t_{\text{He}}$ . To quantitatively express the impact of the presence of HNO<sub>3</sub> on ice we have taken the ratio  $J_{\text{ev}}^b$  to  $J_{\text{ev}}^e$ , namely  $r^{b/e}$ , as follows:

$$r^{b/e} = \frac{J_{\text{ev}}^b}{J_{\text{ev}}^e} \quad (8)$$

This ratio brackets  $J_{\text{ev}}$  between a maximum value, namely that of the evaporation of pure ice,  $J_{\text{ev}}^b$ , and a minimum value  $J_{\text{ev}}^e$  that is characteristic of  $J_{\text{ev}}$  of H<sub>2</sub>O at the end of NAT decomposition obtained when the HNO<sub>3</sub> MS signal decreases to the background level after desorption and serves as a rough guide for the impact of HNO<sub>3</sub> on  $J_{\text{ev}}$ .

For the experiment presented in Figure 6 the value of  $r^{b/e}$  is 13.7 which illustrates the extent of the decrease of  $J_{\text{ev}}$  of H<sub>2</sub>O due to the presence of HNO<sub>3</sub> on ice for the above cited protocol of HNO<sub>3</sub> deposition.

#### 4. Additional Results and Discussion

Most of the existing studies dealing with the impact of HNO<sub>3</sub> on ice evaporative rates have been performed in terms of the dependence of the desorption rate of H<sub>2</sub>O on the continuous or timed exposure of the ice film to a certain partial pressure of HNO<sub>3</sub>,<sup>43</sup> or in terms of the type of nitric acid hydrates or coating<sup>16,19,44</sup> without knowledge of the quantities of HNO<sub>3</sub> that were adsorbed on ice as a result of HNO<sub>3</sub> exposure. We are



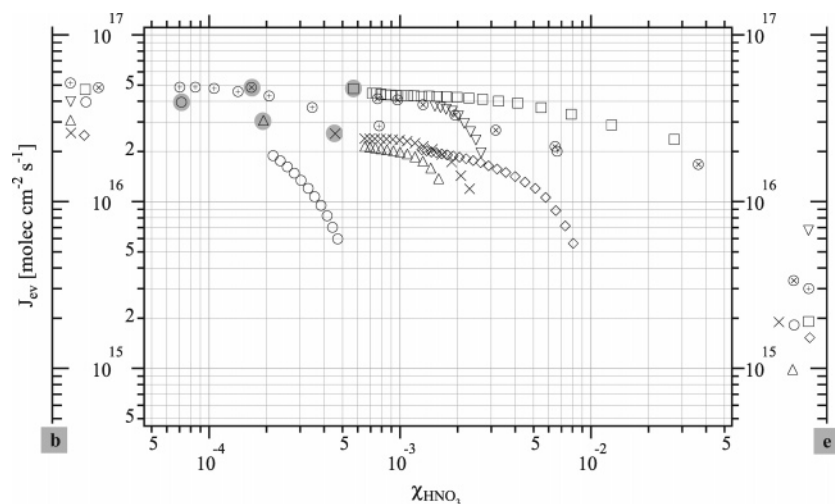


**Figure 7.** Dependence of evaporative flux,  $J_{\text{ev}}$ , of H<sub>2</sub>O on  $\chi_{\text{HNO}_3}$ , for different protocols of HNO<sub>3</sub> deposition on ice in the temperature range 189 <  $T$  < 195 K. Information concerning each experimental set (symbol, rate of deposition and quantity of HNO<sub>3</sub> adsorbed) is listed in Table 2. The significance of axes labeled “b” and “e” is given in the text. The shaded point corresponds to the initial value of  $J_{\text{ev}}$  for a given HNO<sub>3</sub> content.

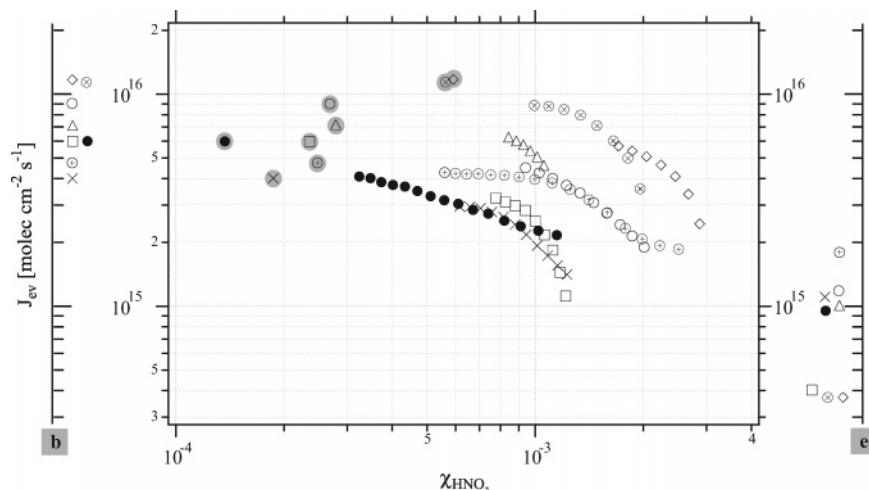


**Figure 8.** Dependence of evaporative flux,  $J_{\text{ev}}$ , of H<sub>2</sub>O on  $\chi_{\text{HNO}_3}$ , for different protocols of HNO<sub>3</sub> deposition on ice in the temperature range 179 <  $T$  < 185 K. Information concerning each experimental set (symbol, rate of deposition and quantity of HNO<sub>3</sub> adsorbed) is listed in Table 2. The significance of axes labeled “b” and “e” is given in the text. The shaded point corresponds to the initial value of  $J_{\text{ev}}$  for a given HNO<sub>3</sub> content.

proposing in this work to examine in close detail the changes of the evaporative flux  $J_{\text{ev}}$  of H<sub>2</sub>O during sublimation of a HNO<sub>3</sub>/H<sub>2</sub>O ice film on the quantities of adsorbed HNO<sub>3</sub> expressed as average mole fraction  $\chi_{\text{HNO}_3}$ .

Several experiments have been performed to study  $J_{\text{ev}}$  of H<sub>2</sub>O in the temperature range 179–208 K. Selected experimental results are presented in Table 2. For the sake of discussion we have arbitrarily broken down the data into three temperature ranges as follows: (a) range 1, 189 <  $T$  < 195 K, data displayed in Figure 7, (b) range 2, 179 <  $T$  < 185 K, data displayed in Figure 8, and (c) range 3, 205 <  $T$  < 208 K, data displayed in Figure 9.

For temperature range 1,  $4.0 \times 10^{13}$  to  $2.2 \times 10^{15}$  molecules of HNO<sub>3</sub> were adsorbed on an ice film in the range 189 to 195 K under stirred flow conditions at a rate of HNO<sub>3</sub> deposition between  $3.1 \times 10^{12}$  to  $3.1 \times 10^{13}$  molecules s<sup>-1</sup>. Figure 7 displays the change of  $J_{\text{ev}}$  of H<sub>2</sub>O during ice film evaporation as a function of increasing average  $\chi_{\text{HNO}_3}$  for the different cases presented in Table 2 under range 1. The values of  $J_{\text{ev}}^{\text{b}}(\text{H}_2\text{O})$  and  $J_{\text{ev}}^{\text{e}}(\text{H}_2\text{O})$  are plotted on the left axis labeled “b” and on the right axis labeled “e”, respectively. The former is reported on the graph itself at the actual initial value of  $\chi_{\text{HNO}_3}$  and corresponds to the shaded points. Therefore, the first (shaded)

data point in each series describes the actual starting point of the individual evaporation history of each HNO<sub>3</sub>/H<sub>2</sub>O sample. The last plotted point corresponds to the thin evaporating film at  $t_{\text{th}}$  just before the onset of HNO<sub>3</sub> evaporation. The common trend in the cases presented in Figure 7 is a continuous albeit nonlinear decrease of  $J_{\text{ev}}$  starting at  $J_{\text{ev}}^{\text{b}}$  and ending at  $J_{\text{ev}}^{\text{e}}$  during ice film evaporation regardless of the deposition conditions. In most cases  $J_{\text{ev}}$  first decreases “slowly” before coming to a “fast” decrease with increasing  $\chi_{\text{HNO}_3}$ . To identify the nature of the adsorbed HNO<sub>3</sub> on ice we have calculated the equivalent partial pressure of HNO<sub>3</sub>,  $P_{\text{HNO}_3}$ , required to maintain the measured rate of HNO<sub>3</sub> deposition listed in Table 2. It was calculated using the uptake coefficient  $\gamma$  of HNO<sub>3</sub> on ice in the range 180–211 K<sup>46</sup> and is listed in Table 3.

The main conclusion from Table 3 is that for all the cases presented in this work the predominant HNO<sub>3</sub> species that was formed during deposition on ice is nitric acid trihydrate (NAT, HNO<sub>3</sub>·3H<sub>2</sub>O) in agreement with the published HNO<sub>3</sub>/H<sub>2</sub>O phase diagram.<sup>45</sup> This prediction is confirmed by spectroscopic studies that have been performed using the same deposition conditions and the FTIR window as support (Si).<sup>22</sup> These FTIR spectra in transmission shown in Figure 10 will be used as supporting evidence below. We claim that the systematic formation of nitric



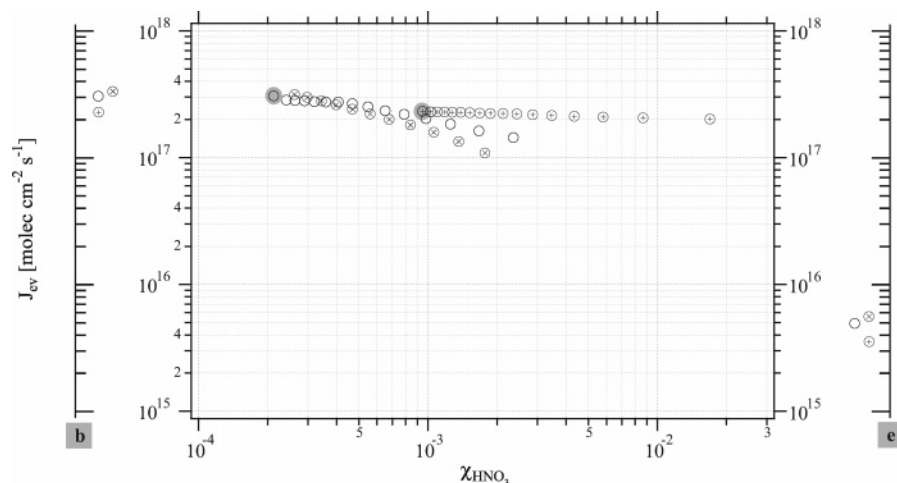


**Figure 9.** Dependence of evaporative flux,  $J_{ev}$ , of  $H_2O$  on  $\chi_{HNO_3}$ , for different protocols of  $HNO_3$  deposition on ice in the temperature range  $205 < T < 208$  K. Information concerning each experimental set (symbol, rate of deposition and quantity of  $HNO_3$  adsorbed) is listed in Table 2. The significance of axes labeled “b” and “e” is given in the text. The shaded point corresponds to the initial value of  $J_{ev}$  for a given  $HNO_3$  content.

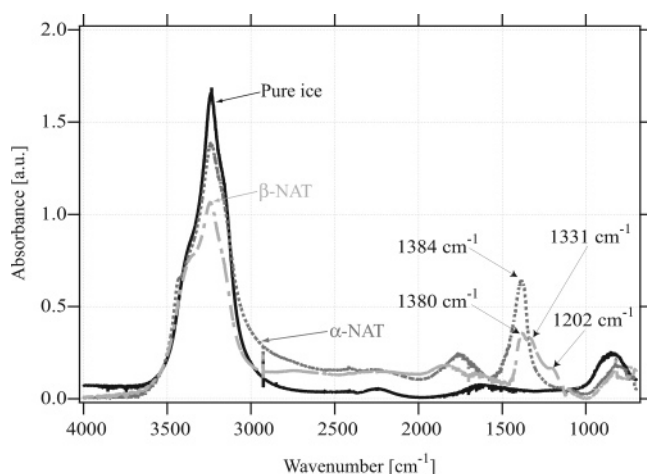


**Figure 10.** Typical transmission FTIR spectra recorded during experiments to evaluate the impact of the deposition of  $HNO_3$  on the vapor pressure of  $H_2O$  upon ice. The black spectrum corresponds to pure  $I_h$  ice deposited at 190 K before  $HNO_3$  doping. The dark gray trace corresponds to the remaining  $H_2O$  and  $HNO_3$  film just before the change in  $H_2O$  vapor pressure occurred in the reactor at point A in Figure 15. The light gray trace identified as  $\beta$ -NAT appears just after the sudden change in the increasing pressure which begins at point labeled A in Figure 15.

**TABLE 3: Partial Pressure of  $HNO_3$  Required to Result in the Measured Rate of  $HNO_3$  deposition,  $R_{HNO_3}$ , Listed in Column 4 and Also Given in Column 5 in Table 2**

$T$ range [K]	expt no.	$T_{ice}$ [K]	$R_{HNO_3}$ [molecules $s^{-1}$ ]	$\gamma^{46}$	$P_{HNO_3}$ [Torr]	predicted surface species <sup>45</sup>
189–195	5	195	$3.1 \times 10^{12}$	0.22	$1.1 \times 10^{-7}$	NAT
	7	189	$3.1 \times 10^{13}$	0.26	$9.7 \times 10^{-7}$	NAT
179–185	12	180	$5.5 \times 10^{12}$	0.30	$1.5 \times 10^{-7}$	NAT
	18	185	$2.2 \times 10^{13}$	0.29	$6.0 \times 10^{-7}$	NAT
205–208	22	207	$5.6 \times 10^{12}$	0.11	$4.1 \times 10^{-7}$	NAT
	21	207	$3.0 \times 10^{13}$	0.11	$2.2 \times 10^{-6}$	NAT

acid trihydrate NAT in all experiments performed in this work is due to the deposition of  $HNO_3$  under slightly undersaturated conditions relative to  $H_2O$  vapor in agreement with reported results.<sup>45</sup>

A comparison of experiment 15 (symbol  $\otimes$  in Figure 8) presented in Table 2 with the work published by Zondlo et al.<sup>48</sup> leads to the same conclusion that undersaturation of water vapor

may be the key to the formation of crystalline NAT. As a case in point, Zondlo et al. show in their study that the deposition of  $HNO_3$  on an ice film leads to an FTIR spectrum characteristic of a supercooled  $H_2O/HNO_3$  liquid at  $P_{HNO_3} = 5.0 \times 10^{-7}$  Torr. It just so happens that the calculated rate of  $HNO_3$  deposition in that work at 185 K based on the uptake coefficient  $\gamma = 0.29$  of Aguzzi and Rossi<sup>46</sup> closely corresponds to experiment 15 listed in Table 2. In contrast to Zondlo et al.<sup>48</sup> we observe the formation of NAT that is identified using FTIR absorption to be discussed below. The main difference between the work of Zondlo et al. and the present one is that in the former case the deposition of  $HNO_3$  is performed under equilibrium conditions of  $H_2O$  vapor,  $P_{H_2O}^{eq}$ , whereas the latter occurred under conditions of undersaturation of  $H_2O$  vapor at stirred flow, that is at slow pumping conditions leading to  $P_{H_2O}^{ss} < P_{H_2O}^{eq}$ . Moreover, as  $P_{H_2O}$  or the relative humidity was decreased below 100% in the study of Zondlo et al. the FTIR spectrum indicated a change toward the formation of NAT. They claimed that this change was due to the preferential evaporation of  $H_2O$  rather than  $HNO_3$  when the relative humidity decreased which led to an increased concentration of  $HNO_3$  in the ice film and reportedly to NAT formation. We confirm that the undersaturation in  $H_2O$  vapor may be key to the crystallization of NAT during  $HNO_3$  deposition. In support of these conclusions Middlebrook et al. describe the direct nucleation of NAT for conditions of undersaturation of  $P_{H_2O}$ .<sup>47</sup> In addition to our observation that the deposition of  $HNO_3$  systematically leads to the formation of NAT, we have chosen to focus the present kinetic study on the influence of the dose and the rate of deposition of  $HNO_3$  on ice as well as the temperature of deposition.

Similar to the data displayed in Figure 6 we have plotted the values of  $r^{b/e}$  representing the extent of the decrease of  $J_{ev}$  for each experiment presented in Figures 7–9. The resulting  $r^{b/e}$  are displayed in Figures 11 and 12 as a function of  $R_{HNO_3}$  and of the dose of  $HNO_3$ ,  $N_{HNO_3}$ , respectively. Although it is difficult to duplicate both dose,  $N_{HNO_3}$ , and rate of deposition of  $HNO_3$ ,  $R_{HNO_3}$ , exactly, experiments 15 and 18 performed at 185 K and displayed in Figure 8 (symbols  $\otimes$  and  $\diamond$  in Table 2) may be selected to evaluate the reproducibility of the present experiments. Although both dose and rate are approximately 10% larger in experiment 18 ( $\diamond$ ) compared to 15 ( $\otimes$ ) the resulting value for  $r^{b/e}$  is identical to within the uncertainty limit as may be seen in Figures 11 and 12, which thus points to a satisfactory reproducibility.

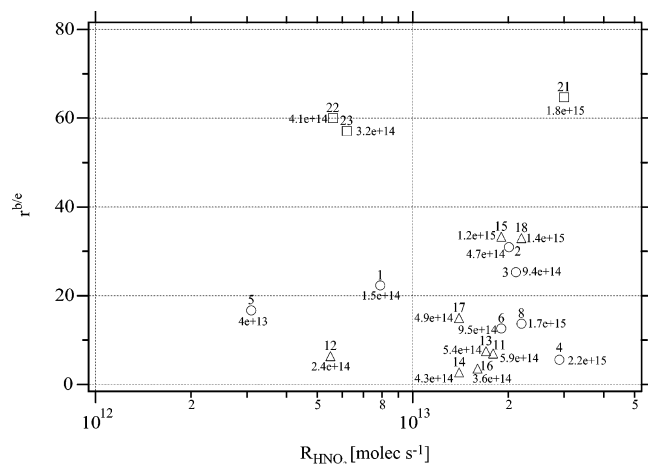


**Figure 11.** Synopsis of the dependence of  $r^{b/e}$  on the rate of deposition  $R_{\text{HNO}_3}$  of  $\text{HNO}_3$  for temperatures between 179 and 208 K. Data (○) apply to 189–195, (△) 179–185, and (□) 205–208 K. Each point is labeled with the total number of  $\text{HNO}_3$  molecules deposited on the ice film and with a number referring to each experiment listed in Table 2.

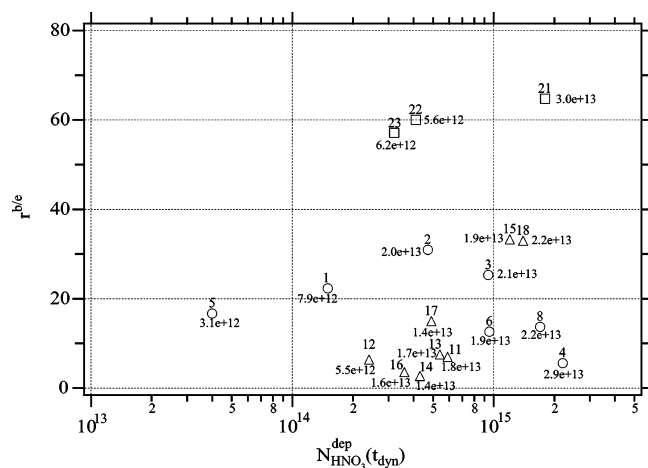


**Figure 12.** Synopsis of the dependence of  $r^{b/e}$  on the adsorbed number of  $\text{HNO}_3$ ,  $N_{\text{HNO}_3}(t_{\text{dyn}})$ , dispensed on ice for temperatures between 179 and 208 K. Data (○) apply to 189–195, (△) 179–185, and (□) 205–208 K. Each point is labeled with the deposition rate of  $\text{HNO}_3$  molecules in molecules  $\text{s}^{-1}$  on the ice film and with a number referring to each experiment listed in Table 2.

In search of the experimental parameters controlling the mole fraction ( $\chi_{\text{HNO}_3}$ ) dependence displayed in Figures 7–9 the parameter  $r^{b/e}$  bracketing the beginning and the end of a thin film evaporation experiment has been plotted as a function of the logarithm of  $R_{\text{HNO}_3}$  and  $N_{\text{HNO}_3}^{\text{dep}}(t_{\text{dyn}})$  in Figures 11 and 12. Because the distribution of the  $r^{b/e}$  values is practically identical in both figures to within experimental accuracy we come to the conclusion that  $R_{\text{HNO}_3}$  and  $N_{\text{HNO}_3}^{\text{dep}}(t_{\text{dyn}})$  are not independent parameters controlling the observable  $r^{b/e}$ . Both  $R_{\text{HNO}_3}$  and  $N_{\text{HNO}_3}^{\text{dep}}(t_{\text{dyn}})$  are interconnected by the deposition time  $t_{\text{dep}}$  through  $R_{\text{HNO}_3} \times t_{\text{dep}} = N_{\text{HNO}_3}^{\text{dep}}(t_{\text{dyn}})$  or the time integral of  $R_{\text{HNO}_3}$  in case it is not constant.

To a first approximation temperature seems to be the most important controlling parameter for  $r^{b/e}$  with which it scales in some fashion. The  $r^{b/e}$  values for range 3 (205–208 K) are approximately 60 whereas they are between 3 and 15 for range 2 (179–185 K) with intermediate values for range 1. There are two apparent exceptions, namely  $r^{b/e}$  values for experiments 15 and 18 as well as for experiment 4. The latter value seems too low for range 1, whereas the former values pertaining to range 2 seem too high although the temperature of 185 K is close to

189 K, the lower bound of range 1. Even within a given range the increase of temperature affects  $r^{b/e}$  in a significant way which may become apparent when considering the increase of  $r^{b/e}$  of experiment 6 (189 K) and 3 (193 K). It seems that the details of the concentration dependence of  $J_{\text{ev}}$  depend in a complex way on several parameters, and the effect of  $t_{\text{dep}}$  and  $R_{\text{HNO}_3}$  on  $r^{b/e}$  would seem to be a starting point for a systematic study yet to be undertaken. Specifically, the “outlier” experiment 4 leading to low values of  $r^{b/e}$  discussed above is also the one performed at the highest value of  $R_{\text{HNO}_3}$  suggesting an inverse dependence of  $r^{b/e}$  on  $R_{\text{HNO}_3}$ . In fact, experiments 3, 6, 8, and 4 of range 1 displayed in Figure 12 lead to lower values of  $r^{b/e}$  compared to the maximum for experiment 2. It is also this group of experiments that has been performed at distinctly higher values of  $R_{\text{HNO}_3}$  compared to experiments 5 and 1 to the left of the maximum, experiment 2, small temperature differences within range 1 notwithstanding. In summary, temperature undoubtedly seems to be an important parameter as well as  $R_{\text{HNO}_3}$ ,  $N_{\text{HNO}_3}^{\text{dep}}(t_{\text{dyn}})$ , and  $t_{\text{dep}}$  or a combination thereof. However, the exact functional dependence of  $r^{b/e}$  on these three parameters will have to be studied in more detail in the future.

These conclusions have helped us understand the results of Zondlo et al.<sup>48</sup> concerning the decrease of the rate of evaporation of  $\text{H}_2\text{O}$  from ice in the presence of  $\text{HNO}_3$  upon deposition. They claimed to have measured a small decrease in  $J_{\text{ev}}$  of 40% relative to pure ice. Indeed, we confirm a  $J_{\text{ev}}$  value from their data that is a factor of 1.7 smaller than for pure ice at 0% relative humidity. Using their conditions for deposition of  $\text{HNO}_3$  on ice, namely  $1.0 \times 10^{-5}$  Torr of  $\text{HNO}_3$  at  $T = 192$  K and dynamic equilibrium in conjunction with the uptake coefficient obtained by Aguzzi and Rossi<sup>46</sup> ( $\gamma = 0.23$  at 192 K) we arrive at  $N_{\text{HNO}_3}^{\text{dep}}(t_{\text{dyn}}) = 2.8 \times 10^{15}$  molec and  $R_{\text{HNO}_3} = 2.8 \times 10^{14}$  molecules  $\text{s}^{-1}$ . Owing to the trend observed in the present study where increasing values of  $R_{\text{HNO}_3}$  lead to a decrease of  $r^{b/e}$  we would expect a decrease of  $r^{b/e}$  to a value lower than 5.6 which is measured in experiment 4 displayed in Figure 11. Thus, the low observed value of  $r^{b/e} = 1.7$  observed by Zondlo et al. would confirm the trend of a decrease of  $r^{b/e}$  with increasing  $R_{\text{HNO}_3}$  given the fact that  $R_{\text{HNO}_3}$  used in experiment 4 is just a factor of 10 lower than in Zondlo et al. whereas  $N_{\text{HNO}_3}^{\text{dep}}$  is approximately the same in both cases.

In addition to these kinetic considerations we have investigated the trend in the dependence of the thickness of ice affected by the presence of  $\text{HNO}_3$ , which should be of prime interest in atmospheric science. We have therefore investigated the influence of both  $N_{\text{HNO}_3}(t_{\text{dyn}})$  and  $R_{\text{HNO}_3}$  on  $d_{\text{D}}$  defined as the thickness of pure ice below which  $J_{\text{ev}}$  decreases by 15% relative to pure ice, namely  $J_{\text{ev}} < 0.85J_{\text{ev}}(\text{pure ice})$ . Values for  $d_{\text{D}}$  are given in Table 2, and Figures 13 and 14 show the dependence of  $d_{\text{D}}$  on  $R_{\text{HNO}_3}$  and  $N_{\text{HNO}_3}(t_{\text{dyn}})$ , respectively.

Similar to the effort of searching for the significant parameters controlling  $r^{b/e}$  discussed above we have plotted  $d_{\text{D}}$  as a function of  $R_{\text{HNO}_3}$  and  $N_{\text{HNO}_3}(t_{\text{dyn}})$  in Figures 13 and 14. Despite the considerable scatter in the plots the temperature seems to group the  $d_{\text{D}}$  values into broad categories where high and low temperatures correlate with low and high values of  $d_{\text{D}}$ , respectively, in an inverse relationship. If one takes the data of range 1 from Table 2, or simply the two limiting experiments 5 and 4 one may be left with the suggestion that a large  $\text{HNO}_3$  deposition rate or dose may lead to a large value of  $d_{\text{D}}$ . This may point to an increasing role of  $\text{HNO}_3$  diffusion into ice with increasing dose or deposition rate.

In agreement with the observed inverse temperature relationship of  $d_{\text{D}}$  the present data lead to the conclusion that the 1

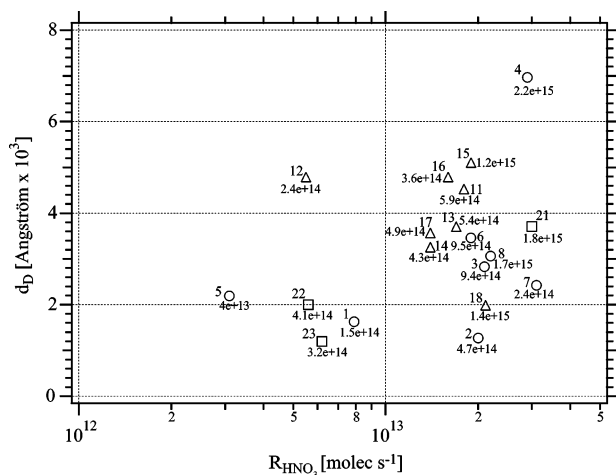


**Figure 13.** Synopsis of the dependence of  $d_D$  on the rate of deposition  $R_{\text{HNO}_3}$  of  $\text{HNO}_3$  for temperatures between 179 and 208 K. Data (O) apply to 189–195, ( $\Delta$ ) 179–185, and ( $\square$ ) 205–208 K. Each point is labeled with the total number of  $\text{HNO}_3$  molecules,  $N_{\text{HNO}_3}^{\text{dep}}$ , deposited on the ice film and with a number referring to each experiment listed in Table 2.

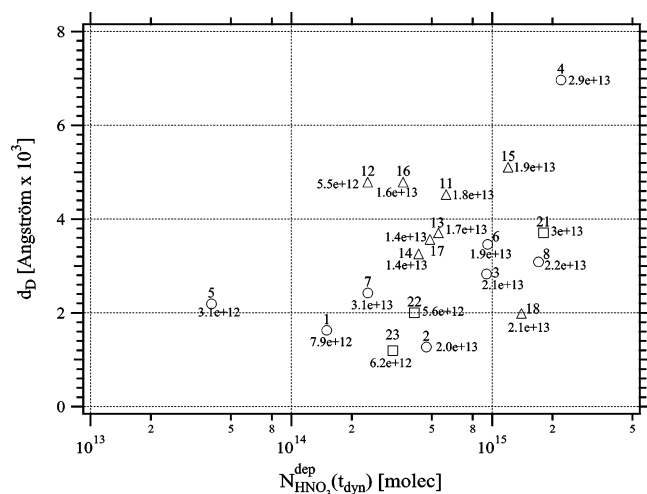


**Figure 14.** Synopsis of the dependence of  $d_D$  on the adsorbed number of  $\text{HNO}_3$ ,  $N_{\text{HNO}_3}(t_{\text{dyn}})$ , dispensed on ice for temperatures between 179 and 208 K. Data (O) apply to 189–195, ( $\Delta$ ) 179–185, and ( $\square$ ) 205–208 K. Each point is labeled with the deposition rate of  $\text{HNO}_3$  in molecules  $\text{s}^{-1}$ ,  $R_{\text{HNO}_3}$ , on the ice film and with a number referring to each experiment listed in Table 2.

$\mu\text{m}$  thick  $\text{HNO}_3$ -doped ice films evaporating at low temperatures (range 2) lead to a  $d_D$  value of  $0.40 \pm 0.10 \mu\text{m}$  whereas the high-temperature data (range 3) lead to  $d_D = 0.25 \pm 0.14 \mu\text{m}$ . This then leads to the qualitative conclusion that the spatial extent of the doped ice film whose  $\text{H}_2\text{O}$  evaporation rate is up to 15% lower than that for pure ice, is increasing with temperature owing to the increasing role of  $\text{HNO}_3$  diffusion in the ice film.

Fahey et al.<sup>17</sup> report the detection of large  $\text{HNO}_3$ -containing particles in the winter Arctic stratosphere at altitudes between 16 and 21 km. On the basis of their experimental conditions of 16–21 km altitude,  $\text{H}_2\text{O}$  and  $\text{HNO}_3$  mixing ratios of 5 ppmv and 9 ppbv, respectively, and a temperature of 192 K and on the basis of the measured uptake coefficient for  $\text{HNO}_3$  on ice<sup>46</sup> of  $\gamma = 0.23$  at 192 K, we calculate an equivalent rate of deposition of  $\text{HNO}_3$ ,  $R_{\text{HNO}_3}$ , of  $1.5 \times 10^{13}$  molecules  $\text{s}^{-1}$  in our experimental chamber which closely corresponds to experiment 2 in Table 2 that is labeled with the  $\Delta$  symbol in Figure 7. Notwithstanding the fact that experiment 2 has been performed

at a slightly larger value of  $R_{\text{HNO}_3}$ , and lower temperature (190 instead of 192 K) compared to the field experiment reported by Fahey et al. we claim that laboratory experiment 2 displayed in Figure 7 comes quite close to explaining the existence of NAT-“coated” ice particles in the atmosphere. The kinetic results suggest a significantly lower value for  $J_{\text{ev}}$  of  $\text{H}_2\text{O}$  with increasing  $\chi_{\text{HNO}_3}$ . It will eventually decrease to the limiting low value of  $J_{\text{ev}}$  in agreement with  $r^{b/e} = 30.9$ . The decrease of  $J_{\text{ev}}$  will lead to small but persistent NAT-containing ice particles that will rapidly grow under conditions of  $\text{H}_2\text{O}$  supersaturation.

In addition to the study of the kinetics of evaporation of  $\text{H}_2\text{O}$  from a  $\text{HNO}_3$ -contaminated ice film we have performed a FTIR spectroscopic investigation of the species that form on ice films when the typical rate and dose for  $\text{HNO}_3$  deposition presented in Table 2 are applied. The Si window of the cryostat was used for ice deposition<sup>22</sup> as was the directed injection of  $\text{HNO}_3$ .

The FTIR spectrum presented in Figure 10 results from the deposition of a  $1.7 \mu\text{m}$  thick ice film on the Si-window at a rate of  $1.0 \times 10^{17}$  molecules  $\text{cm}^{-2} \text{s}^{-1}$  at 190 K under static conditions. Subsequently, the system was set to stirred flow conditions and  $\text{HNO}_3$  was deposited on top of the ice film by directed injection in position  $\text{DT}_{\text{HNO}_3}^{\text{Si}}$ . The rate of deposition of  $\text{HNO}_3$  was  $7.0 \times 10^{14}$  molecules  $\text{s}^{-1}$  to a total number of adsorbed  $\text{HNO}_3$  of  $4.1 \times 10^{17}$  corresponding to approximately 200 formal monolayers. The temperature of the doped ice film was increased at a rate of  $4 \text{ K min}^{-1}$  in this nonisothermal experiment and the pressure in the static reactor was monitored using the Baratron pressure gauge (Figure 1, item 12). In Figure 10, the black trace represents the FTIR spectrum recorded at the beginning of the experiment without  $\text{HNO}_3$  on the ice film under static conditions at 190 K. It corresponds to pure thermodynamically stable  $I_h$  ice.

The dark gray trace exhibiting a sharp peak at  $1384 \text{ cm}^{-1}$  typical of metastable  $\alpha$ -NAT corresponds to the last FTIR spectrum recorded for  $\text{HNO}_3$ -doped ice before the decrease of  $P_{\text{H}_2\text{O}}$  relative to the equilibrium vapor pressure  $P_{\text{H}_2\text{O}}^{\text{eq}}$  over pure ice. This will be discussed in more detail below.

Indeed, during most of the ice film evaporation with increasing temperature  $P_{\text{H}_2\text{O}}$  corresponds to the equilibrium vapor pressure of  $\text{H}_2\text{O}$ ,  $P_{\text{H}_2\text{O}}^{\text{eq}}$ , despite the large  $\text{HNO}_3$  dose applied. To illustrate this point, Figure 15 shows the change of  $P_{\text{H}_2\text{O}}$  in the reactor (light gray trace) when the temperature of the ice film is increased. The necessary thermal transpiration corrections of  $P_{\text{H}_2\text{O}}$  measured using a Baratron pressure gauge caused by the difference in temperature between the ice sample and the reactor wall have been applied according to reference 22. The black  $\bullet$  symbol displays the values for  $P_{\text{H}_2\text{O}}^{\text{eq}}$  over ice from Marti and Mauersberger.<sup>57</sup> Up to 205 K at point A,  $P_{\text{H}_2\text{O}}$  in the reactor in the presence of a  $\text{HNO}_3$ -doped ice film is in excellent agreement with the  $P_{\text{H}_2\text{O}}^{\text{eq}}$  values of Marti and Mauersberger for pure ice. Beyond  $T > 205 \text{ K}$ ,  $P_{\text{H}_2\text{O}}$  was less than  $P_{\text{H}_2\text{O}}^{\text{eq}}$ .

We have performed several sets of evaporation experiments using the Si-window in order to check the identity of the  $\text{HNO}_3$  species when deposited on the ice film. The signature of the deposit on the Si-window was always monitored using FTIR absorption spectroscopy in transmission. Using the same conditions for ice growth and doping with  $\text{HNO}_3$  as the one for deposition on the QCM sensor we have been able to confirm that in all cases formation of NAT occurred when  $\text{HNO}_3$  was deposited on ice under stirred flow conditions. The typical absorption at  $1384 \text{ cm}^{-1}$  of NAT and more generally FTIR spectra between 700 and  $4000 \text{ cm}^{-1}$  were in good agreement with previously published spectroscopic results<sup>49–56</sup> for NAT, so-called  $\alpha$ -NAT. Figure 10 presents a typical FTIR spectrum



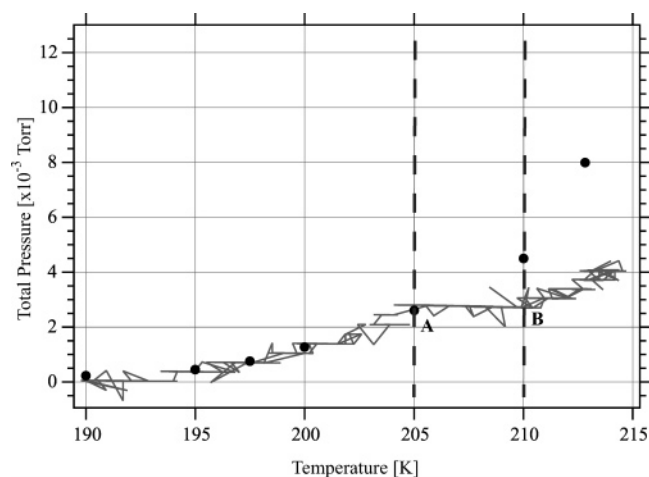


**Figure 15.** Change in  $P_{\text{H}_2\text{O}}$  in the presence of ice for the experiment that leads to the FTIR spectra given in Figure 10. Experimental deposition conditions are  $4.1 \times 10^{17}$  molecules of HNO<sub>3</sub>. The light gray trace corresponding to the measured pressure in the reactor follows the  $\bullet$  symbol representing  $P_{\text{H}_2\text{O}}^{\text{eq}}$  on pure ice of Marti and Mauersberger<sup>57</sup> up to point A. The plateau in the pressure observed between points A and B corresponds to the conversion of  $\alpha$ - to  $\beta$ -NAT as shown in Figure 10.

that perfectly agrees with the literature spectra but was recorded in the final stage of evaporation of a HNO<sub>3</sub>-doped ice film where  $J_{\text{ev}}$  was low.

In Figure 10, the black trace corresponds to the FTIR spectrum of the pure ice film before doping with HNO<sub>3</sub>. Subsequently, the film is doped with roughly 200 monolayers of HNO<sub>3</sub> at a rate of  $7.0 \times 10^{14}$  molecules s<sup>-1</sup> at 190 K and the temperature is increased under static conditions as explained previously. First, the FTIR spectrum of the doped ice exhibits the characteristic band of absorption of  $\alpha$ -NAT (dark gray trace in Figure 10). The decrease of the absorbance in the OH-stretch region ( $3236 \text{ cm}^{-1}$ ) is mainly due to the decrease of the thickness of the doped ice film in order to maintain  $P_{\text{H}_2\text{O}}^{\text{eq}}$  in the static reactor when the temperature increases. When the ice film containing 200 monolayers of HNO<sub>3</sub> reached the temperature of 205 K at point A in Figure 15 the pressure increase was halted with increasing temperature of the film up to point B at 210 K before increasing again. The light gray trace in Figure 10 showing 3 peaks at 1380, 1331, and  $1202 \text{ cm}^{-1}$  is representative of the FTIR spectrum of  $\beta$ -NAT just after point A in Figure 15 was reached. This spectrum has been attributed to other species of NAT in previous studies.<sup>52</sup> The conversion of crystalline NAT from the metastable  $\alpha$ - to the stable  $\beta$ -form may be responsible for the change of the FTIR spectrum during the temperature increase as identified in previous studies.<sup>47,58,59</sup> This observation may be correlated with the data of Koehler<sup>44</sup> who also report a rapid conversion from  $\alpha$ - to  $\beta$ -NAT during TPD experiments, albeit at lower temperatures. It seems that under our experimental conditions the metastable  $\alpha$ -NAT is formed with increasing total pressure  $P_{\text{H}_2\text{O}}^{\text{eq}}$  before reaching point A in Figure 15, whereas the conversion from  $\alpha$ - to the stable  $\beta$ -NAT takes place just after point A on the flat portion of the  $P_{\text{H}_2\text{O}}^{\text{eq}}$  curve.

Using the parameters given in Table 1 for the optical cryostat such as the surface of the silicon window of  $0.78 \text{ cm}^2$ , the optical density of ice of 1.08 corresponding to a thickness of  $10000 \text{ \AA}$ , and data published by Middlebrook et al.<sup>54</sup> on the ability for HNO<sub>3</sub> inclusions to inhibit ice evaporation, we have calculated the average mole fraction  $\chi_{\text{HNO}_3}$  at point A in Figure 15. Middlebrook et al. have calibrated the optical density, OD, at

$1384 \text{ cm}^{-1}$  of  $\alpha$ -NAT in order to measure the thickness of NAT films and found  $\text{OD}_{1384}/\text{thickness} = 0.728 \text{ \AA}^{-1}$ . Using this result we have calculated the thickness of  $\alpha$ -NAT given by the dark gray trace displayed in Figure 10 to be  $8600 \text{ \AA}$ . In 1952, Luzzati<sup>60</sup> measured the density of NAT as  $1.65 \text{ g cm}^{-3}$  based on crystallographic measurements. This value combined with the previously calculated thickness of  $8600 \text{ \AA}$  gives a total number of  $5.7 \times 10^{17}$  formula units of NAT in the examined sample where all adsorbed HNO<sub>3</sub> molecules would be implied in NAT formation as observed by the FTIR spectrum. This value is larger by approximately 20% than the one we obtained using the standard method for the determination of the number of HNO<sub>3</sub> molecules deposited onto ice, namely  $4.1 \times 10^{17}$  molecules, given previously. Using data for pure ice<sup>23</sup> we have calculated that the dark gray spectrum representing HNO<sub>3</sub>-doped ice ( $\alpha$ -NAT) in Figure 10 corresponds to  $3.3 \times 10^{18}$  molecules of H<sub>2</sub>O if we use the optical density of 1.4 units at the peak of the O–H stretch of H<sub>2</sub>O in  $\alpha$ -NAT of  $3236 \text{ cm}^{-1}$ . This leads to  $\chi_{\text{HNO}_3} = 0.17$  which seems to be required to induce a phase change in going from a HNO<sub>3</sub>/H<sub>2</sub>O mixture toward NAT including its associated change of  $P_{\text{H}_2\text{O}}^{\text{eq}}$  from point A to higher temperatures (Figure 15). This last result is of importance because in the case of Figure 10 HNO<sub>3</sub> is far more concentrated compared to all other experiments presented in this study. Conversely, this also means that  $P_{\text{H}_2\text{O}}^{\text{eq}}$  of pure ice may be observed in the chamber roughly to point A of Figure 15 before an incipient phase change from  $\alpha$ - to  $\beta$ -NAT.

In summary, owing to the sets of experiments presented in this work, it appears that the used deposition conditions of HNO<sub>3</sub> onto pure ice, namely the rate of deposition,  $R_{\text{HNO}_3}$ , and the number of HNO<sub>3</sub> molecules deposited,  $N_{\text{HNO}_3}^{\text{dep}}$ , control the time dependence of the evaporative flux of H<sub>2</sub>O,  $J_{\text{ev}}$ , from the doped ice film. As was the case for the presence of HCl on ice,<sup>22</sup> we are able to distinguish three different kinds of H<sub>2</sub>O molecules in the doped ice film. First, right after the end of the doping process a certain number of H<sub>2</sub>O molecules, corresponding to the thickness  $d_{\text{D}}$  of the ice film, evaporate at a rate characteristic of pure ice and are apparently not influenced by the presence of HNO<sub>3</sub>. Second, remaining H<sub>2</sub>O molecules are “trapped” in the ice film and lead to an evaporative flux,  $J_{\text{ev}}$  that continuously decreases as the number of H<sub>2</sub>O molecules in the ice film decreases, concomitantly with increasing  $\chi_{\text{HNO}_3}$ . The evaporation of all these remaining H<sub>2</sub>O molecules is influenced by the presence of HNO<sub>3</sub>, even if they are not directly involved in the  $\alpha$ -NAT structure that is revealed by FTIR spectroscopy. Of utmost importance, the evaporation/condensation of most of these “trapped” H<sub>2</sub>O molecules of c-ice leads to an equilibrium vapor pressure in the presence of a HNO<sub>3</sub>-doped ice film that is that of pure ice. This result implies that the rate of condensation of H<sub>2</sub>O onto the doped ice film should decrease to the same extent as  $J_{\text{ev}}$  in order to achieve thermochemical closure. Finally, as  $\chi_{\text{HNO}_3}$  increases to values higher than  $0.17 \pm 0.09$ , we have observed that the equilibrium vapor pressure of H<sub>2</sub>O over the doped ice film no longer is that of pure ice but leads to a lower value (starting at point B in Figure 15).

In light of recent airborne measurements of water vapor together with HNO<sub>3</sub>, both in natural cirrus as well as aviation contrails in the upper troposphere, Gao et al.<sup>16</sup> came to the conclusion that a new ice particle, so-called  $\Delta$ -ice was responsible for relative humidities in the neighborhood of 135% below 202 K. Unfortunately, the superb field observations of in situ detection of both gas phase and condensed phase HNO<sub>3</sub> together with vapor phase H<sub>2</sub>O expressed as relative humidities were interpreted by invoking the breakdown of microscopic revers-



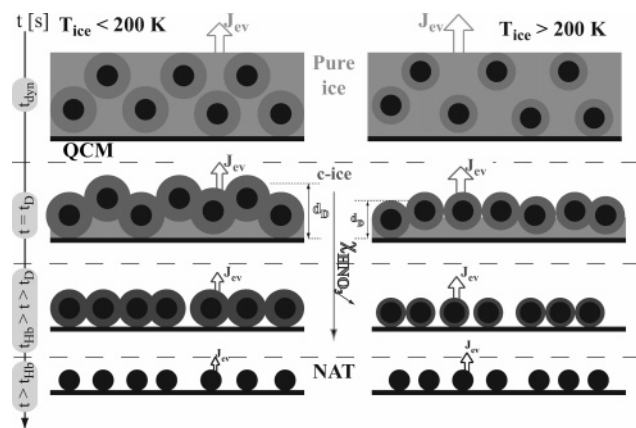


**Figure 16.** Scenario of the change of the evaporative flux,  $J_{ev}$ , of  $H_2O$  with the average mole fraction,  $\chi_{HNO_3}$ . The light gray area corresponds to the presence of “free” water molecules that are predominant at the beginning of the ice film evaporation and lead to  $J_{ev}$  of pure ice. The full black circles represent the NAT “clusters” forming after deposition of  $HNO_3$  onto ice that are influencing the evaporative flux of the c-ice water molecules represented by the dark gray circles. From top to bottom of the drawing  $\chi_{HNO_3}$  increases whereas  $J_{ev}$  decreases.

ibility. They assumed that  $\gamma$  for  $H_2O$  condensation decreased but that in turn  $J_{ev}$  was unchanged in going from pure ice to ice doped with a fraction of a monolayer of  $HNO_3$  in order to explain an increased equilibrium vapor pressure in agreement with the measured  $H_2O$  supersaturation. This diodelike behavior of the ice substrate has been shown to lead to a perpetual mobile of the second kind.<sup>21</sup> In the following, we would like to show that the field data of Gao et al.<sup>16</sup> may be interpreted using the results of this study in terms of a slow approach to the known equilibrium vapor pressure  $P_{H_2O}^{eq}$  that may occur on a time scale of several tens of minutes which may exceed the time scale of the field observation.

The dependence of  $J_{ev}$  on  $\chi_{HNO_3}$  in the high-temperature range 205–208 K (range 3) presented in Figure 9 displays at most a decrease of  $J_{ev}$  by a factor of 2 when considering the difference between pure ice and the last displayed value that corresponds to point  $t_{Hb}$  in the evaporation-time history of Figure 4. It is important to recall that the measured vapor pressure in this range corresponds to that of pure ice,  $P_{H_2O}^{eq}$ , despite the decrease of  $J_{ev}$ . This puts a powerful thermodynamic constraint on the rate of condensation,  $k_{cond}$  or  $\gamma$ , which has been experimentally verified.<sup>23</sup> In contrast,  $J_{ev}$  for the low (range 2, Figure 8) and intermediate (range 1, Figure 7) temperature range which both satisfy  $T < 200$  K shows a much larger relative decrease as a function of  $\chi_{HNO_3}$  with respect to pure ice of up to a factor of 7 as exemplified by data series 1 at  $T = 191$  K in Table 2, which is displayed in Figure 7.

One type of  $H_2O$  present in an ice film containing a small amount of  $HNO_3$  corresponds to free ice evaporating first at  $J_{ev}$  characteristic of pure ice of thickness  $d_0$  from this part of the thin film not affected by the presence of  $HNO_3$  and corresponds to the initial part of the evaporation-time history of thin film ice as displayed in Figure 4 from  $t = 0$  to  $t = 160$  s. The second is called complexed water ice (c-ice) and is characterized by decreasing  $J_{ev}$  values and  $P_{H_2O}^{eq}$ , the value of pure ice at  $T$ . Figure 16 presents a qualitative scenario of the temporal change of the predominant  $H_2O$  molecules that evaporate. We use a kinetic parameter ( $J_{ev}$ ) in order to distinguish between the two types of ice because both have the same value of  $P_{H_2O}^{eq}$ . The decrease of  $J_{ev}$  of  $H_2O$  spans the transition from free ice to c-ice and occurs over an average increase of  $\chi_{HNO_3}$  on the order of a factor of 10–100 as displayed

in Figures 7 and 8. It corresponds to a smooth transition between free ice and c-ice which most likely indicates the presence of an amorphous mixture between  $H_2O$  and  $HNO_3$  rather than a stoichiometric phase such as  $\alpha$  or  $\beta$ -NAT. The reason for refraining to plot further values of  $J_{ev}$  at higher  $\chi_{HNO_3}$  or at evaporation times exceeding  $t_{Hb}$  lies in the simultaneous evaporation of both  $HNO_3$  and  $H_2O$  which renders the evaluation of  $\chi_{HNO_3}$  difficult.

We make the assumption that the present data on ice films may be transferred to the evaporation history of ice particles at temperatures that overlap with Gao et al.<sup>16</sup> It is clear from the foregoing that c-ice is observable at  $T < 200$  K and that the condensation rate constant  $k_{cond}$  or  $\gamma$  for  $H_2O$  vapor decreases to the same extent as  $J_{ev}$  displayed in Figures 7, 8, and 9 owing to the constant value of  $P_{H_2O}^{eq}$  up to  $t_{Hb}$ , the last data point corresponding to the highest value of  $\chi_{HNO_3}$ . We will now estimate the first-order rate constant  $k_{cond}$  for condensation of  $H_2O$  for the conditions of the field observations of Gao et al. assuming that the significantly higher rh values are a remnant of previous higher temperatures in the sampled air mass and that  $P_{H_2O}^{eq}$  is relaxing to its equilibrium value with a characteristic relaxation time  $1/k_{cond}$ . The present results enable one to obtain a quantitative answer in terms of  $k_{cond}$  as a function of  $T$  and surface area density (SAD) of atmospheric ice. Using typical SAD values of natural cirrus clouds ranging from  $10^2$  to  $10^4$   $\mu m^2/cm^3$  corresponding to  $10^{-6}$  to  $10^{-4}$   $cm^2/cm^3$  as given by Gao et al. and a typical spread in  $\gamma$  for  $H_2O$  of  $\gamma = 10^{-2}$  to  $10^{-3}$  at 200 K from this work and Delval et al.,<sup>22,23</sup> we arrive at a value of  $k_{cond}$  in the range  $1.2 \times 10^{-4}$  to  $1.2 \times 10^{-2}$   $s^{-1}$  using  $k_{cond} = \gamma(c/4)SAD$ , where  $c = 485$   $m s^{-1}$  is the average molecular speed of  $H_2O$  at 200 K. The relaxation time spans a range from 23 h to 1.4 min using both the spread in SAD and  $\gamma$  values, noting in passing that mass transport considerations are probably not of importance here owing to the small ice particle sizes and the magnitude of  $\gamma$ . Considering the fact that three to five relaxation periods are needed in order to effectively establish  $H_2O$  vapor equilibrium we come to the conclusion that the field observations of Gao et al. may have been influenced by long  $H_2O$  vapor relaxation times and that there may be no need to invoke a new phase of ice having an increased vapor pressure relative to pure ice upon adsorption of a fractional monolayer of  $HNO_3$ . By carefully inspecting the rh values of Gao et al. one may note the large variability of the collected data which adds weight to the relaxation time argument as the airborne platform samples air that is close to equilibrium to various extents. The short relaxation times estimated in the work of Gao et al. therefore do not seem to be consistent with the present results.

One of the corollaries of the present work is the presence of complexed  $H_2O$  on  $HNO_3$ -containing ice films whose evaporation rate is significantly smaller, but whose vapor pressure is that of pure ice,  $P_{H_2O}^{eq}$ . We thus arrive at the conclusion that three distinguishable types of  $H_2O$  are present on  $HNO_3$ -containing ice films under our laboratory conditions: free  $H_2O$  whose  $J_{ev}$  is that of pure ice, complexed (c)  $H_2O$  and  $H_2O$  over NAT. The first two have an equilibrium  $H_2O$  vapor pressure that is that of pure ice,  $P_{H_2O}^{eq}$ .

**Acknowledgment.** We would like to thank the Fonds National Suisse de la Recherche Scientifique for generous support under Project No. 20-65299.01 and 200020-105471/1.

#### Appendix A. Calibration of $HNO_3$ Dosing of the Ice Film

The first step relies on the calibration of the MS signal of  $HNO_3$  at  $m/z = 30$  which enables a 1:1 correspondence between

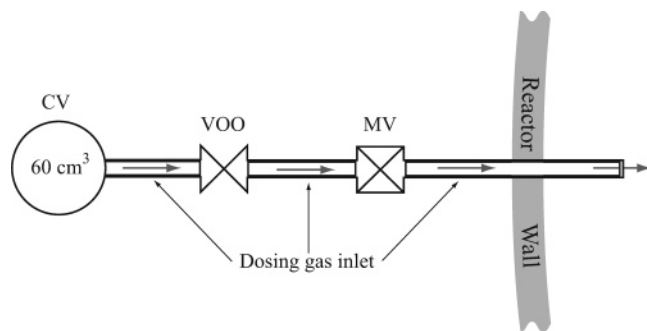


**Figure 17.** Schematic drawing of the gas admission line: VOO allows the effusion of the trace gas (HNO<sub>3</sub>) from the  $V_c = 60 \text{ cm}^3$  Teflon-coated calibrated volume (CV) through the dosing tube and across the metering valve MV into the reactor.

MS intensities  $I_{30}$  and the partial pressure or concentration of HNO<sub>3</sub> in the chamber.

Under stirred flow conditions (gate valve closed, leak valve open) the calibration of  $I_{30}$  is based on establishing the ratio between the MS signal and the partial pressure of HNO<sub>3</sub>,  $P_{\text{HNO}_3}$ , in the upper chamber that is measured using the Baratron absolute pressure gauge (Figure 1, item 12). HNO<sub>3</sub> is admitted into the reactor through the dosing tube in position DT<sub>HNO<sub>3</sub></sub><sup>QCM</sup> such that the following equalities hold for the flow of HNO<sub>3</sub> from the reactor chamber to the MS analysis chamber at a flow rate  $F_r(\text{HNO}_3)$ :

$$F_r(\text{HNO}_3) = \frac{P_{\text{HNO}_3} \times V_r}{R \times T_r} \times k_{\text{esc}}(\text{HNO}_3) \quad (9)$$

$$= [\text{HNO}_3] \times V_r \times k_{\text{esc}}(\text{HNO}_3) \quad (10)$$

$$= \text{Conv} \times V_r \times k_{\text{esc}}(\text{HNO}_3) \times P_{\text{HNO}_3} \quad (11)$$

$$= C_{30}^{\text{s-flow}} \times I_{30} \quad (12)$$

where Conv is the conversion factor between the partial pressure and the concentration of HNO<sub>3</sub> in the chamber in molec Torr<sup>-1</sup> cm<sup>-3</sup> (Table 1),  $P_{\text{HNO}_3}$  the pressure of HNO<sub>3</sub> in Torr,  $V_r$  the volume of the reactor in cm<sup>3</sup>, and  $k_{\text{esc}}(\text{HNO}_3)$ , the rate of effusion of HNO<sub>3</sub> through the calibrated leak in s<sup>-1</sup>.  $I_{30}$  corresponds to the intensity of the MS signal for  $m/z = 30$  in A and  $C_{30}^{\text{s-flow}}$  is the calibration factor for  $m/z = 30$  under stirred flow conditions in molecules s<sup>-1</sup> A<sup>-1</sup>. By combining eqs 11 and 12 and measuring both  $P_{\text{HNO}_3}$  and  $I_{30}$ , we may evaluate  $C_{30}^{\text{s-flow}}$  following eq 13:

$$C_{30}^{\text{s-flow}} = \text{Conv} \times V_r \times k_{\text{esc}}(\text{HNO}_3) \times \frac{P_{\text{HNO}_3}}{I_{30}} \quad (13)$$

Under dynamic conditions (gate valve open)  $C_{30}^{\text{dyn}}$  is evaluated using the decrease of the pressure of HNO<sub>3</sub> in the Teflon-coated calibrated volume (CV, volume  $V_c$ ),  $P_{\text{HNO}_3}$ , used as a reservoir for the HNO<sub>3</sub> flow into the reactor when the ON/OFF valve, VOO, displayed in Figure 17 is opened. The correspondence between the measured  $\Delta P_{\text{HNO}_3}/\Delta t$  and the MS signal at  $m/z = 30$  yields  $C_{30}^{\text{dyn}}$ , the calibration factor for  $m/z = 30$  under dynamic conditions in eq 14 by analogy with eq 13:

$$C_{30}^{\text{dyn}} = \text{Conv} \times V_c \times \frac{\Delta P_{\text{HNO}_3}}{\Delta t} \times \frac{1}{I_{30}} \quad (14)$$

The calibration factors for  $m/z = 30$  and  $m/z = 18$ , namely  $C_{30}^{\text{s-flow}}$ ,  $C_{18}^{\text{s-flow}}$ ,  $C_{30}^{\text{dyn}}$  and  $C_{18}^{\text{dyn}}$ , are all determined using the same method and are listed in Table 1.

The smallest measurable MS signal for HNO<sub>3</sub> at  $m/z = 30$  at a signal-to-noise ratio  $S/N = 2:1$  is of the order of  $8.0 \times 10^{-14}$  A. Using the appropriate calibration factor for  $m/z = 30$ , this limit leads to the smallest measurable flow rate of  $4.9 \times 10^{12}$  molecules s<sup>-1</sup> under stirred flow conditions. Under dynamic conditions the detection limit is approximately  $1.0 \times 10^{-13}$  A leading to the minimum measurable flow rate of  $2.2 \times 10^{12}$  molecules s<sup>-1</sup>.

The second step in the evaluation of the absolute amount of HNO<sub>3</sub> deposited on the ice substrate consists of taking the difference of  $I_{30}$  under stirred flow conditions, with and without an ice film on the QCM. This difference in MS signals may be converted into an absolute number of HNO<sub>3</sub> molecules that have been deposited onto the ice film located on the QCM quartz sensor compared to the few HNO<sub>3</sub> molecules sticking to the quartz sensor set at 320 K (Table 1).

The glass tubing used for the directed injection of HNO<sub>3</sub> was aimed at the center of the QCM sensor and connected to the ON/OFF valve (VOO), as displayed in Figure 17, which itself is located upstream of the micrometer dosing valve MV (Swagelok double pattern low-pressure metering valves with vernier handle of type SS-SS2-D-TVVH, valves denoted  $V_1$  and  $V_2$ ). Figure 17 presents a schematic illustration of the injection line where VOO separates the Teflon-coated calibrated volume used as a reservoir for HNO<sub>3</sub> from MV. For a given pressure of HNO<sub>3</sub> of approximately 2 Torr in the calibrated volume we have systematically established the correspondence between the aperture of MV and  $I_{30}$ . We subsequently have compared  $I_{30}$  when the QCM sensor is at ambient temperature (no ice) and in the presence of an ice film at the same experimental settings of pressure and aperture of  $V_1$  and  $V_2$  of MV. Using the appropriate calibration factor, the time integration of the difference between both  $I_{30}$  signals enables the measurement of the loss of gas-phase HNO<sub>3</sub> owing to the deposition of HNO<sub>3</sub> on the ice substrate thanks to the certainty that there is no cold spot in the chamber other than the QCM sensor as shown in reference 23.

Figure 3 illustrates a specific case of a HNO<sub>3</sub> deposition on a 1.2 μm thick ice substrate at  $T_{\text{ice}} = 189 \text{ K}$  with apertures of the double metering valve MV set to  $V_1 = V_2 = 15$  units and with  $P_{\text{HNO}_3}^0 = 2034 \text{ mTorr}$  in the Teflon coated calibrated volume CV under stirred flow conditions. Previously, the film was deposited by condensation of water vapor under static conditions at 190 K at a rate of  $1 \times 10^{17}$  molecules cm<sup>-2</sup> s<sup>-1</sup>. Subsequently the temperature of the film was set to the desired value, 189 K in this example.

At  $t = t_0 = 0 \text{ s}$  in Figure 3, VOO is opened, allowing the effusion of HNO<sub>3</sub> from the reservoir CV across MV and the tubing into the reactor. The gray trace  $I_{30}$  corresponds to the case where the QCM is at 320 K (no ice) which is used as a reference for the deposition of HNO<sub>3</sub> on top of the ice film. The black trace  $I_{30}$  corresponds to the identical case as above for deposition of HNO<sub>3</sub> on the ice film between  $t_0$  and  $t_e = 74 \text{ s}$  which corresponds to the end of the dosing period when the reactor is set to dynamic conditions and VOO is closed. Indeed, by analogy with the case of HCl described in detail in ref 22 we have checked that the directed deposition of dopants onto ice under stirred flow conditions leads to a residual pressure of the doping gas that is low enough to prevent competitive deposition from the chamber. This is all the more the case in the present example where the system is set to molecular flow

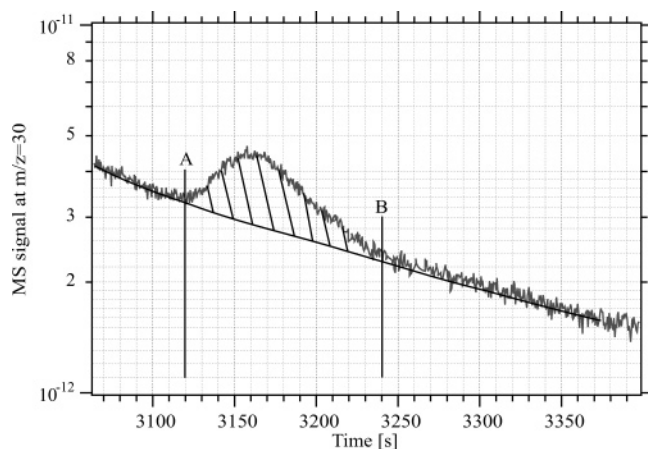


**Figure 18.** Typical MS signal at  $m/z = 30$  during evaporation of an ice film from the QCM, here at  $T = 189$  K. The hatched area limited by points A and B is proportional to the number of  $\text{HNO}_3$  molecules evaporating from the ice surface and corresponds to  $1.8 \times 10^{15}$  molecules of  $\text{HNO}_3$ .

conditions once the end of the chosen deposition time has been reached at  $t_e$ . Depending on the total pressure in the upper chamber the MS was sometimes turned off just when the system was set from stirred flow to dynamic conditions in order to protect the MS filament from an occasional sudden pressure surge. In the case presented above we have chosen to display only the time period during which  $\text{HNO}_3$  direct deposition occurs.

The hatched area in Figure 3 represents the absolute loss of gas-phase  $\text{HNO}_3$  in the presence of the ice film compared to the reference experiment with no ice. As the piezoelectric sensor is the unique cold target in the reactor this loss therefore corresponds to the number of  $\text{HNO}_3$  molecules deposited onto ice. Thus, the difference between both  $I_{30}$  signals at  $t < 74$  s obtains the rate,  $R_{\text{HNO}_3}$ , of  $\text{HNO}_3$  adsorption on the ice film. The time integration of this difference in the  $m/z = 30$  MS signals between  $t = 0$  ( $t_0$ ) and 74 s ( $t_e$ ) yields the absolute number of  $\text{HNO}_3$  molecules,  $N_{\text{HNO}_3}^{\text{dep}}$ , present on the ice substrate. For the case of Figure 3  $(1.7 \pm 0.2) \times 10^{15}$  molecules of  $\text{HNO}_3$  have been deposited during 74 s at an average rate of  $2.2 \times 10^{13}$  molecules  $\text{s}^{-1}$ .

Figure 18 shows  $I_{30}$  during the evaporation of the ice film that was the substrate for  $\text{HNO}_3$  condensation in Figure 3. The hatched area limited by points A and B corresponds to evaporating  $\text{HNO}_3$  molecules,  $N_{\text{HNO}_3}^{\text{evap}}$ , which in the present case corresponds to  $(1.8 \pm 0.2) \times 10^{15}$  molecules of  $\text{HNO}_3$ . This value is in excellent agreement with the value obtained previously during deposition and corresponds to a satisfied mass balance.

For each of the experiments presented in this work, the mass balance was routinely established between  $\text{HNO}_3$  deposited on the ice film measured using the above-mentioned method and  $\text{HNO}_3$  recovered in the process of evaporation of the  $\text{H}_2\text{O}/\text{HNO}_3$  ice film. The mass balance varied in all the cases within less than a factor of 2.1 which corresponds to the worst case. Table 2 summarizes several experiments performed in this study using different rates of deposition as well as different doses of  $\text{HNO}_3$ .

## References and Notes

- (1) Voigt, C.; Schreiner, J.; Kohlmann, A.; Zink, P.; Mauersberger, K.; Larsen, N.; Deshler, T.; Kroger, C.; Rosen, J.; Adriani, A.; Cairo, F.; Di Donfrancesco, G.; Viterbini, M.; Ovarlez, J.; Ovarlez, H.; David, C.; Dornbrack, A. *Science* **2000**, 290, 1756–1758.
- (2) Solomon, S.; Garcia, R. R.; Rowland, F. S.; Wuebbles, D. J. *Nature* **1986**, 321, 755–758.
- (3) McElroy, M. B.; Salawitch, R. J.; Wofsy, S. C.; Logan, J. A. *Nature* **1986**, 321, 759–762.
- (4) Wylie, D. P.; Menzel, W. P. *J. Climate* **1999**, 12 (1), 170–184.
- (5) Wang, P. H.; Minnis, P.; McCormick, M. P.; Kent, G. S.; Skeens, K. M. *J. Geophys. Res.-Atmos.* **1996**, 101 (D23), 29407–29429.
- (6) Penner, J. E.; Intergovernmental Panel on Climate Change. Working Group I; Intergovernmental Panel on Climate Change. Working Group III. *Aviation and the global atmosphere: a special report of IPCC Working Groups I and III in collaboration with the Scientific Assessment Panel to the Montreal Protocol on Substances that Deplete the Ozone Layer*; Cambridge University Press: Cambridge, 1999.
- (7) Kley, D.; Russell, J. M., III; Phillips, C., Eds. *SPARC Assessment of Upper Tropospheric and Stratospheric Water Vapour*; World Climate Research Programme no. 113, World Meteorological Organisation/TD no. 1043, SPARC Report no. 2, 2000.
- (8) Liou, K. N. *Mon. Weather Rev.* **1986**, 114, 1167–1199.
- (9) Borrmann, S.; Solomon, S.; Dye, J. E.; Luo, B. P. *Geophys. Res. Lett.* **1996**, 23, 2133–2136.
- (10) Lawrence, M. G.; Crutzen, P. J. *Tellus Ser. B—Chem. Phys. Meteorol.* **1998**, 50 (3), 263–289.
- (11) Popp, P. J.; Gao, R. S.; Marcy, T. P.; Fahey, D. W.; Hudson, P. K.; Thompson, T. L.; Karcher, B.; Ridley, B. A.; Weinheimer, A. J.; Knapp, D. J.; Montzka, D. D.; Baumgardner, D.; Garrett, T. J.; Weinstock, E. M.; Smith, J. B.; Sayres, D. S.; Pittman, J. V.; Dhaniyala, S.; Bui, T. P.; Mahoney, M. J. *J. Geophys. Res.-Atmos.* **2004**, 109 (D8), Art. No. D08306.
- (12) Neuman, J. A.; Gao, R. S.; Fahey, D. W.; Holecek, J. C.; Ridley, B. A.; Walega, J. G.; Grahek, F. E.; Richard, E. C.; McElroy, C. T.; Thompson, T. L.; Elkins, J. W.; Moore, F. L.; Ray, E. A. *Atmos. Environ.* **2001**, 35, 5789–5797.
- (13) Meier, A.; Hendricks, J. J. *Geophys. Res.-Atmos.* **2002**, 107 (D23), Art. No. 4696.
- (14) Houghton, J. T. *Intergovernmental Panel on Climate Change. Working Group I. Climate change 2001: the scientific basis: contribution of Working Group I to the third assessment report of the Intergovernmental Panel on Climate Change*; Cambridge University Press: Cambridge, U.K., and New York, 2001.
- (15) Neuman, J. A.; Gao, R. S.; Schein, M. E.; Ciciora, S. J.; Holecek, J. C.; Thompson, T. L.; Winkler, R. H.; McLaughlin, R. J.; Northway, M. J.; Richard, E. C.; Fahey, D. W. *Rev. Sci. Instrum.* **2000**, 71, 3886–3894.
- (16) Gao, R. S.; Popp, P. J.; Fahey, D. W.; Marcy, T. P.; Herman, R. L.; Weinstock, E. M.; Baumgardner, D. G.; Garrett, T. J.; Rosenlof, K. H.; Thompson, T. L.; Bui, P. T.; Ridley, B. A.; Wofsy, S. C.; Toon, O. B.; Tolbert, M. A.; Karcher, B.; Peter, T.; Hudson, P. K.; Weinheimer, A. J.; Heymsfield, A. J. *Science* **2004**, 303, 516–520.
- (17) Fahey, D. W.; Gao, R. S.; Carslaw, K. S.; Kettleborough, J.; Popp, P. J.; Northway, M. J.; Holecek, J. C.; Ciciora, S. C.; McLaughlin, R. J.; Thompson, T. L.; Winkler, R. H.; Baumgardner, D. G.; Gandrud, B.; Wennberg, P. O.; Dhaniyala, S.; McKinney, K.; Peter, T.; Salawitch, R. J.; Bui, T. P.; Elkins, J. W.; Webster, C. R.; Atlas, E. L.; Jost, H.; Wilson, J. C.; Herman, R. L.; Kleinbohl, A.; von Konig, M. *Science* **2001**, 291, 1026–1031.
- (18) Biermann, U. M.; Crowley, J. N.; Huthwelker, T.; Moortgat, G. K.; Crutzen, P. J.; Peter, T. *Geophys. Res. Lett.* **1998**, 25, 3939–3942.
- (19) Peter, T.; Muller, R.; Crutzen, P. J.; Deshler, T. *Geophys. Res. Lett.* **1994**, 21, 1331–1334.
- (20) Wofsy, S. C.; Salawitch, R. J.; Yatteau, J. H.; McElroy, M. B.; Gandrud, B. W.; Dye, J. E.; Baumgardner, D. *Geophys. Res. Lett.* **1990**, 17, 449–452.
- (21) McGraw, R. *Science* **2004**, 304, 961–961.
- (22) Delval, C.; Fluckiger, B.; Rossi, M. J. *Atmos. Chem. Phys.* **2003**, 3, 1131–1145.
- (23) Delval, C.; Rossi, M. J. *Phys. Chem. Chem. Phys.* **2004**, 6, 4665–4676.
- (24) Fenter, F. F.; Caloz, F.; Rossi, M. J. *J. Phys. Chem.* **1994**, 98, 9801–9810.
- (25) Neuman, J. A.; Huey, L. G.; Ryerson, T. B.; Fahey, D. W. *Environ. Sci. Technol.* **1999**, 33, 1133–1136.
- (26) Weast, R. C. *CRC Handbook of Chemistry and Physics*, 1st student ed.; CRC Press: Boca Raton, FL, 1988.
- (27) Sadtschenko, V.; Brindza, M.; Chonde, M.; Palmore, B.; Eom, R. J. *Chem. Phys.* **2004**, 121, 11980–11992.
- (28) Dillard, D. S.; Timmerhaus, K. D. In *Thermal Conductivity—Proceedings of the Eighth Conference*; Ho, C.; Taylor, R., Eds.; Plenum Press: New York, 1969.
- (29) Andersson, O.; Johari, J. P.; Huga, H. J. *Chem. Phys.* **2004**, 120, 9612–9617.
- (30) Hessinger, J.; Pohl, R. O. *J. Non-Cryst. Solids* **1996**, 208, 151–161.
- (31) Hessinger, J.; White, B. E.; Pohl, R. O. *Planet Space Sci.* **1996**, 44, 937–944.



- (32) Elvin, A. A.; Connor, J. J.; Choi, D. H. *J. Eng. Mech.-ASCE* **1998**, 124 (1), 54–60.
- (33) Berland, B. S.; Brown, D. E.; Tolbert, M. A.; George, S. M. *Geophys. Res. Lett.* **1995**, 22, 3493–3496.
- (34) Kumai, M. *J. Glaciol.* **1968**, 7, 95–108.
- (35) Bergren, M. S.; Schuh, D.; Sceats, M. G.; Rice, S. A. *J. Chem. Phys.* **1978**, 69, 3477–3482.
- (36) Manca, C.; Martin, C.; Roubin, P. *Chem. Phys.* **2004**, 300, 53–62.
- (37) Schriver-Mazzuoli, L.; Schriver, A.; Hallou, A. *J. Mol. Str.* **2000**, 554, 289–300.
- (38) Lu, C. S.; Lewis, O. *J. Appl. Phys.* **1972**, 43, 4385–4390.
- (39) Pratte, P.; Rossi, M. J. Submitted to *J. Phys. Chem. A*.
- (40) Smith, J. A.; Livingston, F. E.; George, S. M. *J. Phys. Chem. B* **2003**, 107, 3871–3877.
- (41) Thibert, E.; Dominé, F. *J. Phys. Chem. B* **1998**, 102, 4432–4439.
- (42) Zondlo, M. A.; Barone, S. B.; Tolbert, M. A. *J. Phys. Chem. A* **1998**, 102, 5735–5748.
- (43) Warshawsky, M. S.; Zondlo, M. A.; Tolbert, M. A. *Geophys. Res. Lett.* **1999**, 26, 823–826.
- (44) Koehler, B. G. *Int. J. Chem. Kinet.* **2001**, 33, 295–309.
- (45) Worsnop, D. R.; Fox, L. E.; Zahniser, M. S.; Wofsy, S. C. *Science* **1993**, 259, 71–74.
- (46) Aguzzi, A.; Rossi, M. J. *Phys. Chem. Chem. Phys.* **2001**, 3, 3707–3716.
- (47) Middlebrook, A. M.; Berland, B. S.; George, S. M.; Tolbert, M. A.; Toon, O. B. *J. Geophys. Res.-Atmos.* **1994**, 99 (D12), 25655–25666.
- (48) Zondlo, M. A.; Hudson, P. K.; Prenni, A. J.; Tolbert, M. A. *Annu. Rev. Phys. Chem.* **2000**, 51, 473–499.
- (49) Roziere, J.; Potier, J. *J. Inorg. Nucl. Chem.* **1973**, 35, 1179–1183.
- (50) Tolbert, M. A.; Middlebrook, A. M. *J. Geophys. Res.-Atmos.* **1990**, 95 (D13), 22423–22431.
- (51) Smith, R. H.; Leu, M. T.; Keyser, L. F. *J. Phys. Chem.* **1991**, 95, 5924–5930.
- (52) Ritzhaupt, G.; Devlin, J. P. *J. Phys. Chem.* **1991**, 95, 90–95.
- (53) Barton, N.; Rowland, B.; Devlin, J. P. *J. Phys. Chem.* **1993**, 97, 5848–5851.
- (54) Middlebrook, A. M.; Tolbert, M. A.; Drdla, K. *Geophys. Res. Lett.* **1996**, 23, 2145–2148.
- (55) Tisdale, R. T.; Prenni, A. J.; Iraci, L. T.; Tolbert, M. A.; Toon, O. B. *Geophys. Res. Lett.* **1999**, 26, 707–710.
- (56) Escribano, R.; Couceiro, M.; Gomez, P. C.; Carrasco, E.; Moreno, M. A.; Herrero, V. J. *J. Phys. Chem. A* **2003**, 107, 651–661.
- (57) Marti, J.; Mauersberger, K. *Geophys. Res. Lett.* **1993**, 20, 363–366.
- (58) Tolbert, M. A.; Koehler, B. G.; Middlebrook, A. M. *Spectrochim. Acta Part A-Mol. Biomol. Spectrosc.* **1992**, 48, 1303–1313.
- (59) Peil, S.; Seisel, S.; Schrems, O. *J. Mol. Struct.* **1995**, 348, 449–452.
- (60) Luzzati, V. *Acta Crystallogr.* **1953**, 6, 152–157.
- (61) Clouds and the Earth's Radiant Energy System, CERES: URL address: <http://asd-www.larc.nasa.gov/ceres/brochure/brochure.pdf>